**STEPPED WAVEGUIDE ELECTROMAGNETIC MATERIAL
CHARACTERIZATION TECHNIQUE**

THESIS

Sean P. Dorey, Captain, USAF

AFIT/GEO/ENG/04-01

**DEPARTMENT OF THE AIR FORCE
AIR UNIVERSITY**

AIR FORCE INSTITUTE OF TECHNOLOGY

Wright-Patterson Air Force Base, Ohio

AFIT/GEO/ENG/04-01

STEPPED WAVEGUIDE ELECTROMAGNETIC MATERIAL CHARACTERIZATION TECHNIQUE

THESIS

Presented to the Faculty

Department of Electrical and Computer Engineering

Graduate School of Engineering and Management

Air Force Institute of Technology

Air University

Air Education and Training Command

In Partial Fulfillment of the Requirements for the

Degree of Master of Science in Electrical Engineering

Sean P. Dorey, B.S.E.E.

Captain, USAF

March 2004

AFIT/GEO/ENG/04-01

**STEPPED WAVEGUIDE ELECTROMAGNETIC MATERIAL
CHARACTERIZATION TECHNIQUE**

Sean P. Dorey, B.S.E.E.

Captain, USAF

Approved:

_____/signed/_____	23 Feb 04
Dr. Michael J. Havrilla (Chairman)	Date

_____/signed/_____	23 Feb 04
Maj William D. Wood, Ph.D. (Member)	Date

_____/signed/_____	23 Feb 04
Dr. William P. Baker (Member)	Date

Acknowledgments

I would like to express my sincerest gratitude to my advisor and mentor, Dr. Michael Havrilla, for his patient guidance and trust throughout the thesis process. His extraordinary physical intuition and dedication to teaching inspires me to always strive for complete understanding of every problem.

I would also like to thank Major Bill Wood for his help and interest along the way and Dr. William Baker for his close attention to the details of my mathematical expressions.

My sponsor, Dr. Bob Simpson, along with Dr. Jeff Berrie, were a constant source of encouragement and enthusiasm. I am forever indebted to Mr. Rodney George for his technical assistance and generous time spent escorting me as an uncleared visitor during my experimental measurements.

Most importantly, my deepest appreciation goes to my loving wife. Her kind listening skills are a virtue. She is my best friend and favorite fellow AFIT student.

Sean P. Dorey

Table of Contents

List of Figures

List of Tables

AFIT/GEO/ENG/04-01

Abstract

Electromagnetic material characterization is the process of determining the complex permittivity and permeability of a material. A new waveguide material measurement technique is developed to reduce test sample size requirements for low-frequency applications. Specifically, a waveguide sample holder having a reduced aperture is utilized to decrease the time and cost spent producing large precision test samples. This type of sample holder causes a disruption in the waveguide-wall surface currents that results in the excitation of higher-order modes. This thesis will demonstrate how these higher-order modes can be accommodated using a modal-analysis technique, thus resulting in the ability to measure smaller samples mounted in large waveguides and still determine the constitutive parameters of the materials at the desired frequencies.

Experimental results for acrylic and magnetic and electric radar absorbing materials are compared to ideal full-aperture measurements at S-band ($2.6-3.95\text{ GHz}$) to verify the modal-analysis technique. In addition, since uncertainties in test sample thickness and placement are predominantly encountered in material characterization measurements, a differential error analysis is performed to determine associated error bounds.

STEPPED WAVEGUIDE ELECTROMAGNETIC MATERIAL

CHARACTERIZATION TECHNIQUE

1. Introduction

An electromagnetic material is characterized by its permittivity and permeability. In general, the permittivity of a dielectric material determines its susceptibility to becoming polarized when exposed to an electric field. Similarly, the permeability of a magnetic material describes its susceptibility to becoming magnetized when exposed to a magnetic field. Permittivity and permeability are generally both complex quantities, where the real parts are related to energy storage and the imaginary parts are related to the loss mechanisms of the material that convert incident electromagnetic radiation to heat.

A multitude of applications require measurement of the constitutive parameters of an electromagnetic material. For example, consider the following overly simplified process description: 1) electrical engineers specify specific constitutive parameters for a new radar absorbing material (RAM) coating for a stealth aircraft, 2) chemical engineers labor to fabricate the RAM, 3) to test the material formulation, the responsibility returns to the electrical engineers, and 4) the process continues until an acceptable formulation is attained or the original specification is modified. Meanwhile, during this often very time-consuming process, large costs are incurred. This thesis offers a waveguide material

measurement technique aimed at reducing the test sample size requirements for low-frequency applications, and should thus lead to significant time and cost savings.

1.1 *Problem Statement*

Typically, the material characterization process involves several basic steps. First, a test sample is carefully machined to fit into the testing device. Next, the device is connected to a vector network analyzer to obtain the experimentally measured scattering parameters. The network analyzer operates by launching an incident wave towards the test sample and subsequently measuring the amount of signal that is reflected from and transmitted through the material. Finally, numerical algorithms are used to extract the complex permittivity and permeability of the test sample from the experimental S-parameters. The predominant algorithm used to compute the material parameters is the Nicolson-Ross-Weir (NRW) technique [1]-[5].

The NRW technique has the advantage of being one of the few "direct" extraction methods where the material parameters are calculated analytically in closed-form from the experimental S-parameters. Most other extraction methods are "iterative" in nature with an initial guess required to iteratively find the material parameter solutions that satisfy an optimization algorithm.

Test samples must be linear, homogeneous, and isotropic with coplanar front and back surfaces for proper application of the NRW technique. In addition, only a single mode is assumed to be present in the material. Thus, for waveguide applications, the material must completely fill the waveguide cross-section to prevent the excitation of higher-order modes. For frequencies greater than several gigahertz, producing test

samples is relatively simple. In an X-band ($8.2-12.4$ GHz) waveguide, for example, test sample dimensions in the cross-sectional plane are only 0.9 by 0.4 inches. However, for lower-frequency applications waveguide dimensions become progressively larger. Consequently, larger quantities of materials are required leading to possible sample fabrication difficulties.

To overcome these large test sample fabrication difficulties imposed by the NRW technique for low-frequency waveguide measurements, solutions in the past have been to only partially fill the cross-section of the sample holder and perform an analysis using higher-order longitudinal section electric (LSE) or longitudinal section magnetic (LSM) propagating modes [6],[7]. While the LSE/LSM approach reduces the test sample size requirements, it suffers three main drawbacks. First, the higher-order mode propagation constants must be found numerically by solving transcendental equations. Second, it is difficult to associate the propagation constants with the correct modes. And third, this iterative method is very sensitive to the initial guesses for the constitutive parameters.

The goal of this thesis is to eliminate the difficulties in dealing with a partially filled waveguide cross-section by completely filling a sample holder having a reduced aperture. Unlike the LSE/LSM approach, it will be shown that the reduced-aperture sample holder leads to well-known, closed-form expressions for the propagation constants and their associated modes. Specifically, the higher-order modes that result from the disruption of the waveguide-wall surface currents when encountering the waveguide-feed/sample-holder junctions will be accommodated through a modal-analysis technique.

1.2 Limitations

While the modal-analysis technique is much easier to implement than the LSE/LSM approach due to its closed-form solutions, there are limitations that must be understood. Specifically, high-loss materials measured in greatly reduced apertures will lead to transmission coefficients that approach the noise floor of the network analyzer. The poor transmission coupling will in turn significantly degrade the material parameter extraction process. Thus, with high-loss materials of greatly reduced test sample sizes, partially filling a full-aperture sample holder and accounting for the higher-order LSE/LSM modes will lead to better transmission responses, but at the cost of solving complicated transcendental equations. As with any engineering problem, there are tradeoffs to using different approaches.

1.3 Scope

Many other measurement devices can be utilized for material characterization (including, but certainly not limited to, coaxial transmission lines, free-field measurement systems, strip transmission lines, microstrip field applicators, and cavity resonators), but this thesis will explore only rectangular waveguide applications. In addition, only S-band ($2.6 - 3.95\ \mathrm{GHz}$) measurement results will be presented as a proof-of-concept demonstration. However, the stepped waveguide modal-analysis technique will be developed in a general manner that is fully adaptable to the low-frequency measurements for which it was designed.

1.4 Thesis Organization

Chapter 2 provides a theoretical background focusing on transverse electric (TE) modes in rectangular waveguides and wave transmission matrices for analysis of multi-layer environments. Chapter 3 derives the modal-analysis technique that allows a smaller test sample to be mounted in a large waveguide and still determine the constitutive parameters of the material at the desired frequencies. Chapter 4 presents several experimental results that verify the modal-analysis technique. In addition, a differential error analysis related to uncertainties in measuring test sample thickness and placement within the sample holder is conducted in Chapter 4 to form error bounds on the extracted material parameters. Finally, a brief set of conclusions and recommendations for future research are given in Chapter 5.

2. Background

This chapter provides the background necessary for understanding the modal analysis method used in this thesis to accommodate the stepped-waveguide structure. Specifically, modes of rectangular waveguides and wave transmission matrices will be briefly reviewed. Although some minor specializations have been made, an experienced reader familiar with both of these concepts should be able to skip to the next chapter without loss of understanding.

2.1 TE Modes of Rectangular Waveguides

Perfectly conducting rectangular waveguides can support Transverse Electric (TE) and Transverse Magnetic (TM) modes. Most practical waveguide systems are designed to operate so that only the dominant TE_{10} propagating mode is excited because it is the lowest-order mode and thus prevents the possibility of dispersion from higher-order propagating modes. Since TE_{10} mode excitation was used for all laboratory measurements in this thesis, discussion will be limited to developing the pertinent field expressions for TE modes. The interested reader can obtain a more general review of guided-wave theory in Collin [6].

2.1.1 Helmholtz Wave Equation.

The most fundamental beginning to any electromagnetic analysis is Maxwell's Equations. For a linear, homogenous, isotropic material in a source free region, the time

harmonic representation (with a suppressed $e^{j\omega t}$ time dependence) of Maxwell's equations are given by

$$\nabla \times \vec{E} = -j\omega\mu\vec{H} \tag{2.1}$$

$$\nabla \times \vec{H} = j\omega\varepsilon\vec{E} \tag{2.2}$$

$$\nabla \cdot \vec{E} = 0 \tag{2.3}$$

$$\nabla \cdot \vec{H} = 0 \tag{2.4}$$

where $\vec{E}, \vec{H}$ are the electric and magnetic field intensity vectors which are functions of position and angular frequency ω, and ε, μ are the effective permittivity and permeability of the medium which are, in general, also complex functions of angular frequency ω. To uncouple Maxwell's equations, the vector identity $\nabla \times \nabla \times \vec{V} = \nabla(\nabla \cdot \vec{V}) - \nabla^2\vec{V}$ (where $\vec{V}$ is an arbitrary vector) is used to obtain the time harmonic, homogenous Helmholtz vector wave equations

$$\left(\nabla^2 + k^2\right)\begin{Bmatrix}\vec{E}\\\vec{H}\end{Bmatrix} = 0 \tag{2.5}$$

where the complex wave number $k = \omega\sqrt{\varepsilon\mu}$.

In dealing with wave-guiding structures, it is convenient to break up the Helmholtz equation into its transverse and longitudinal components for ease of identifying TE and TM mode solutions. To start, the electric and magnetic fields must also be separated into their respective transverse and longitudinal parts. For forward and reverse propagating waves along the z-axis, the fields can be expressed as

$$\vec{E}(\vec{r}) = \vec{E}(\vec{\rho}, z) = \vec{E}_t(\vec{\rho}, z) \pm \hat{z}E_z(\vec{\rho}, z) = \vec{e}_t(\vec{\rho})e^{\mp\gamma z} \pm \hat{z}e_z(\vec{\rho})e^{\mp\gamma z} \tag{2.6}$$

$$\vec{H}(\vec{r}) = \vec{H}(\vec{\rho}, z) = \pm \vec{H}_t(\vec{\rho}, z) + \hat{z}H_z(\vec{\rho}, z) = \pm \vec{h}_t(\vec{\rho})e^{\mp \gamma z} + \hat{z}h_z(\vec{\rho})e^{\mp \gamma z} \qquad (2.7)$$

where γ is the propagation constant, the position vectors $\vec{r} = (x, y, z)$ and $\vec{\rho} = (x, y)$,

and the subscripts t, z are used to represent the transverse and longitudinal components,

respectively [8]. For TE modes, in which $e_z = 0$, Maxwell's equations reduce to the

following expressions upon equating the transverse and longitudinal field components

$$\gamma \hat{z} \times \vec{e}_t = j\omega\mu \vec{h}_t \qquad (2.8)$$

$$\nabla_t \times \vec{e}_t = -\hat{z}j\omega\mu h_z \qquad (2.9)$$

$$\hat{z} \times \nabla_t h_z + \gamma \hat{z} \times \vec{h}_t = -j\omega\varepsilon \vec{e}_t \qquad (2.10)$$

$$\nabla_t \times \vec{h}_t = 0 \qquad (2.11)$$

$$\nabla_t \cdot \vec{e}_t = 0 \qquad (2.12)$$

$$\nabla_t \cdot \vec{h}_t = \gamma h_z \qquad (2.13)$$

where $\nabla = \nabla_t + \hat{z}\frac{\partial}{\partial z}$ and the vector identity $\nabla \times s\vec{V} = \nabla s \times \vec{V} + s\nabla \times \vec{V}$ (where s is an

arbitrary scalar) are used. Using the vector identity $\vec{A} \times \vec{B} \times \vec{C} = \vec{B}(\vec{A} \cdot \vec{C}) - \vec{C}(\vec{A} \cdot \vec{B})$, the

transverse field components $\vec{e}_t, \vec{h}_t$ can also be expressed in terms of the longitudinal

component h_z as

$$\vec{h}_t = -\frac{\gamma}{k_c^2}\nabla_t h_z \qquad (2.14)$$

$$\vec{e}_t = -Z_{TE}\hat{z} \times \vec{h}_t \qquad (2.15)$$

where the TE wave impedance is given by

$$Z_{TE} = \frac{j\omega\mu}{\gamma} \tag{2.16}$$

Using $\nabla^2 = \nabla_t^2 + \frac{\partial^2}{\partial z^2}$, the wave equation for $\vec{H}$ can now be decomposed into its

transverse and longitudinal components

$$\nabla_t^2 \vec{h}_t(\vec{\rho}) + k_c^2 \vec{h}_t(\vec{\rho}) = 0 \tag{2.17}$$

$$\nabla_t^2 h_z(\vec{\rho}) + k_c^2 h_z(\vec{\rho}) = 0 \tag{2.18}$$

where

$$k_c^2 = \gamma^2 + k^2 \tag{2.19}$$

2.1.2 Separation-of-Variables and Boundary Condition Enforcement.

It has just been shown that if h_z is known, all the field components of TE modes

can be generated using (2.14) and (2.15). Therefore, solution to the scalar wave equation

for h_z given by (2.18) will be sought using the separation-of-variables technique. With

the product solution $h_z(\vec{\rho}) = h_z(x, y) = X(x)Y(y)$ assumed, (2.18) becomes

$$Y(y)\frac{d^2 X(x)}{dx^2} + X(x)\frac{d^2 Y(y)}{dy^2} + k_c^2 X(x)Y(y) = 0 \tag{2.20}$$

and then dividing by $X(x)Y(y)$ gives,

$$\overbrace{\frac{1}{X(x)}\frac{d^2 X(x)}{dx^2}}^{-k_x^2} + \overbrace{\frac{1}{Y(y)}\frac{d^2 Y(y)}{dy^2}}^{-k_y^2} + k_c^2 = 0 \tag{2.21}$$

where the definitions k_x, k_y are made observing that each term of (2.21) must be equal to

a constant, and it is evident that $k_c^2 = k_x^2 + k_y^2$. The solutions to the two separate ordinary

differential equations,

$$\frac{d^2 X(x)}{dx^2} + k_x^2 X(x) = 0$$

$$\frac{d^2 Y(y)}{dy^2} + k_y^2 Y(y) = 0$$

(2.22)

are found considering the rectangular waveguide geometry presented in Figure 2-1, with the origin shifted to the cross-sectional center for mathematical convenience in the next chapter. With the wave bounded in x and y, the appropriate solutions to (2.22) imply the following convenient choice

$$h_z(x, y) = X(x)Y(y) = \left[B_1 \sin\left\{ k_x\left(x + \frac{a}{2}\right) \right\} + B_2 \cos\left\{ k_x\left(x + \frac{a}{2}\right) \right\} \right]$$
$$\times \left[C_1 \sin\left\{ k_y\left(y + \frac{b}{2}\right) \right\} + C_2 \cos\left\{ k_y\left(y + \frac{b}{2}\right) \right\} \right]$$

(2.23)

Imposing the well-known boundary condition that the tangential component of the electric field at a perfectly conducting surface must be zero, expressed mathematically as,

$$\hat{n} \times \vec{E} = 0 \quad \Rightarrow \quad \hat{n} \times \vec{e}_t = 0 \quad \dots \ since \ e_z = 0$$

(2.24)

it can be shown with the help of (2.14) and (2.15) that, at the waveguide walls,

$$\hat{n} \cdot \nabla_t h_z(x, y) = \frac{\partial h_z(x, y)}{\partial n} = 0$$

(2.25)

where $\hat{n}$ is the unit normal vector directed into the field region from the waveguide walls. Enforcing the boundary conditions implied by (2.25), the generating function for TE wave propagation in a rectangular waveguide is given by

$$h_z(x, y) = A_{mn} \cos\left\{ k_x\left(x + \frac{a}{2}\right) \right\} \cos\left\{ k_y\left(y + \frac{b}{2}\right) \right\} , \quad \begin{cases} k_x = \dfrac{m\pi}{a} , \ m = 0,1,2... \\ k_y = \dfrac{n\pi}{b} , \ n = 0,1,2... \end{cases}$$

(2.26)
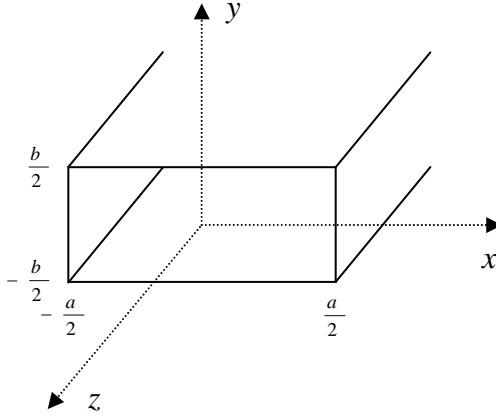
Figure 2-1. Geometry of a rectangular waveguide with the origin placed in the cross-sectional center.

where A_{mn} is the mn^{th} mode amplitude. It must also be noted that m and n cannot both be zero simultaneously, otherwise, upon examination of (2.8)-(2.15), a trivial solution of no wave is reached.

Finally, applying the generating function expressed in (2.26) to (2.14) and (2.15) gives the transverse field equations

$$
\begin{aligned}
e_x &= \frac{j\omega\mu}{k_c^2} A_{mn} k_y \cos\left\{k_x\left(x + \frac{a}{2}\right)\right\} \sin\left\{k_y\left(y + \frac{b}{2}\right)\right\} \\
e_y &= -\frac{j\omega\mu}{k_c^2} A_{mn} k_x \sin\left\{k_x\left(x + \frac{a}{2}\right)\right\} \cos\left\{k_y\left(y + \frac{b}{2}\right)\right\} \\
h_x &= -\frac{e_y}{Z_{TE}} \\
h_y &= \frac{e_x}{Z_{TE}}
\end{aligned}
\tag{2.27}
$$

2.1.3 Cutoff Frequency.

The cutoff frequency of the mn^{th} rectangular waveguide mode is defined by setting the propagation constant of (2.19) to zero:

$$\gamma_{mn} = \sqrt{k_{c,mn}^2 - k^2} = 0 \tag{2.28}$$

Thus, rearrangement of (2.28) gives the cutoff frequency of the TE$_{mn}$ mode as

$$\left(f_{co}\right)_{mn} = \frac{1}{2\pi\sqrt{\varepsilon\mu}}\sqrt{\left(\frac{m\pi}{a}\right)^2 + \left(\frac{n\pi}{b}\right)^2} \quad , \quad \left.\begin{matrix} m = 0,1,2,... \\ n = 0,1,2,... \end{matrix}\right\} \; m = n \neq 0 \tag{2.29}$$

For example, consider a free-space filled S-band waveguide with dimensions

$a = 2.84$ inches and $b = 1.34$ inches. The cutoff frequency for the dominant TE$_{10}$ mode

is 2.078 GHz, while that of the next higher-order mode, the TE$_{20}$ mode, is 4.156 GHz.

S-band waveguides are customarily operated in the frequency range

$1.25 f_{co,10} < f < 0.95 f_{co,20}$ (i.e., $2.6 < f < 3.95$ GHz). This operational regime ensures a

well-behaved dominate propagating mode with all higher-order modes being evanescent.

2.2 Wave Transmission Matrices (A-Parameters)

Wave transmission matrices offer a simple method to deal with multi-layered

environments, and will be utilized in the next chapter to model the sample holder region.

This section will develop individual 2×2 matrices that describe the relationship between

incident and reflected wave amplitudes at a prescribed output terminal plane to those at

the input terminal plane. These individual matrices are then easily cascaded to obtain the

overall wave amplitudes relationships of a multi-layered environment [6].

2.2.1 Geometry of Multi-Layered Environment.

Consider the multi-layered system environment of Figure 2-2 comprised of N

material layers. The respective complex permittivity, permeability, and thickness of the

i^{th} material layer are ε_i, μ_i, and ℓ_i. The complex wave amplitudes of the incident and

2-7

reflected waves within the ith layer are represented by c_i, b_i, respectively. Finally, Γ_i, τ_i

correspond to the Fresnel interfacial reflection and transmission coefficients at the input

plane of the ith layer.

2.2.2 A-Parameter Description of Single Layer.

To analyze the multi-layered system presented in the previous section, it is

necessary to first examine the expanded view of a single layer as shown in Figure 2-3. If

Γ_2, τ_2 and Γ_2', τ_2' are the respective interfacial reflection and transmission coefficients

experienced by waves c_1 and b_2', then the following relations prevail

$$
\begin{aligned}
b_1 &= \Gamma_2 c_1 + \tau_2' b_2' \\
c_2' &= \Gamma_2' b_2' + \tau_2 c_1
\end{aligned}
$$

(2.30)

Then, using the following well-known Fresnel equations (based on continuity of

tangential electric and magnetic fields at the interface)

$$
\begin{aligned}
\tau_2 &= 1 + \Gamma_2 \\
\tau_2' &= 1 + \Gamma_2' \\
\Gamma_2 &= -\Gamma_2' = \frac{Z_2 - Z_1}{Z_2 + Z_1}
\end{aligned}
$$

(2.31)

and a little algebra leads to the matrix expression

$$
\begin{bmatrix} c_1 \\ b_1 \end{bmatrix} = \frac{1}{\tau_2} \begin{bmatrix} 1 & \Gamma_2 \\ \Gamma_2 & 1 \end{bmatrix} \begin{bmatrix} c_2' \\ b_2' \end{bmatrix}
$$

(2.32)

where Z_i is the wave impedance of the ith layer. Thus, (2.32) describes the relationship

between the forward and reverse traveling waves (c_1, b_1) immediately to the left of the

interface to the forward and reverse traveling waves (c_2', b_2') immediately to the right of

the interface.

2-8
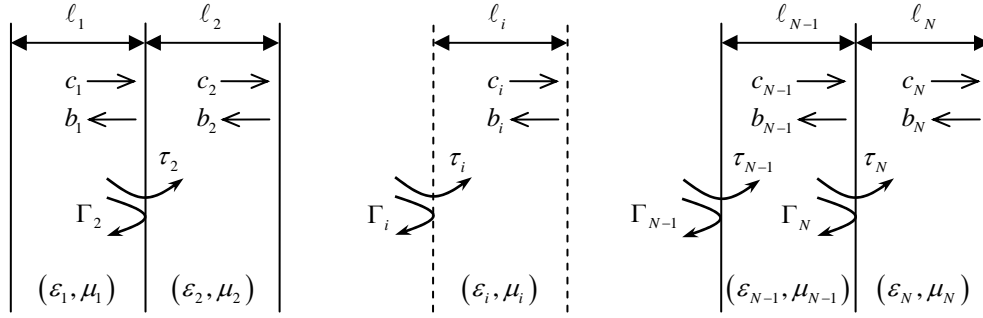
Figure 2-2. Multi-layer environment.
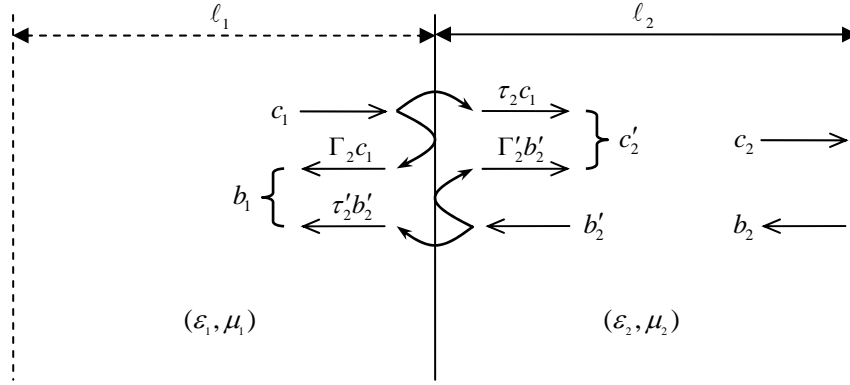
Figure 2-3. Expanded view of a single layer used to demonstrate the reflected and transmitted waves at a planar interface as well as the propagation phase delay.

To complete the matrix description of the layer under consideration, the waves (c_2', b_2') must be related to waves (c_2, b_2) after propagating a distance ℓ_2. Assuming a linear, homogeneous, and isotropic medium, the complex wave amplitude relationships are

$$
\begin{array}{cc}
c_2 = c_2' e^{-\gamma_2 \ell_2} \\
b_2' = b_2 e^{-\gamma_2 \ell_2}
\end{array}
\quad \Rightarrow \quad
\begin{bmatrix} c_2' \\ b_2' \end{bmatrix} =
\begin{bmatrix} e^{\gamma_2 \ell_2} & 0 \\ 0 & e^{-\gamma_2 \ell_2} \end{bmatrix}
\begin{bmatrix} c_2 \\ b_2 \end{bmatrix}
\tag{2.33}
$$

where γ_2 is the propagation constant in layer 2. Finally, combining the results of (2.32) and (2.33) yields

$$\begin{bmatrix} c_1 \\ b_1 \end{bmatrix} = \frac{1}{\tau_2} \begin{bmatrix} e^{\gamma_2 \ell_2} & \Gamma_2 e^{-\gamma_2 \ell_2} \\ \Gamma_2 e^{\gamma_2 \ell_2} & e^{-\gamma_2 \ell_2} \end{bmatrix} \begin{bmatrix} c_2 \\ b_2 \end{bmatrix} = \begin{bmatrix} A_{11} & A_{12} \\ A_{21} & A_{22} \end{bmatrix} \begin{bmatrix} c_2 \\ b_2 \end{bmatrix} \tag{2.34}$$

where the transfer function is normally described in terms of *A-parameters*.

2.2.3 A-Parameter Description of Multi-Layered Environment.

Using the single-layer A-parameter description developed in the previous section, a generalized result can be applied to the multi-layered system of Figure 2-2. The overall A-parameter description of an *N*-layer system is given by the cascaded product of the wave matrices of each individual layer

$$\begin{bmatrix} c_1 \\ b_1 \end{bmatrix} = \prod_{i=2}^{N} \frac{1}{\tau_i} \begin{bmatrix} e^{\gamma_i \ell_i} & \Gamma_i e^{-\gamma_i \ell_i} \\ \Gamma_i e^{\gamma_i \ell_i} & e^{-\gamma_i \ell_i} \end{bmatrix} \begin{bmatrix} c_N \\ b_N \end{bmatrix} = \begin{bmatrix} A_{11} & A_{12} \\ A_{21} & A_{22} \end{bmatrix} \begin{bmatrix} c_N \\ b_N \end{bmatrix} \tag{2.35}$$

where

$$\Gamma_i = \frac{Z_i - Z_{i-1}}{Z_i + Z_{i-1}} \quad , \quad \tau_i = 1 + \Gamma_i \tag{2.36}$$

2.3 Summary

This chapter reviewed TE modes of rectangular waveguides and wave transmission matrices. Understanding of both concepts will form the basis of the modal-analysis technique presented in the next chapter. It will be shown that under TE_{10} mode excitation, the geometry chosen for the reduced-aperture sample holder will cause only specific TE modes to be scattered – no TM modes will need to be considered. Also, the

wave transmission matrix will provide a convenient method to handle measurements of multiple material layers within the sample holder region.

3. Methodology

This chapter presents a modal analysis process that can be used to extract the constitutive material parameters of a test sample mounted in a stepped-waveguide structure from the experimentally measured S-parameters, S_i^{exp}, of a network analyzer. The modal analysis process will be broken up into three simple steps: 1) expand the fields for each region, 2) satisfy boundary conditions across each interface, and 3) test with appropriate integral operators.

The outputs of the modal analysis process are the theoretically calculated S-parameters, S_i^{thy}, for an estimate of the complex relative permittivity and permeability of the test sample. Using an iterative nonlinear least-squares optimization algorithm, the test sample's material parameters will be those that match, within a specified accuracy, the theoretical S-parameters to the experimental values at each frequency:

$$\min\left\{\sum_i \left[S_i^{thy}(\omega,\varepsilon,\mu) - S_i^{exp}(\omega) \right]^2 \right\} \tag{3.1}$$

where $i = 11, 21, 22, 12$.

3.1 Field Expansions

The stepped-waveguide geometry was carefully chosen to simplify the mode-matching process across the waveguide to sample holder interfaces. By matching the reduced aperture of the sample holder to the shape of the TE_{10} mode excitation, mode
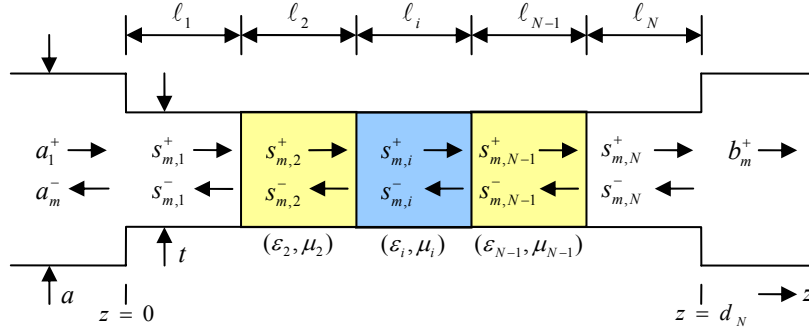
Figure 3-1. Top view stepped-waveguide fixture showing the sample holder region as an N-layer environment.
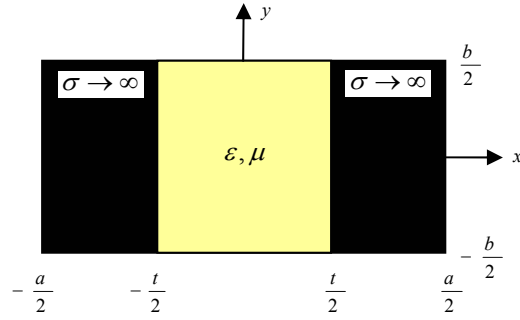
Figure 3-2. Side view of stepped-waveguide fixture.

orthogonality was used to greatly decrease the complexity of the field expansions for the different scattered modes.

3.1.1 Stepped-Waveguide Geometry.

Consider the geometries of Figures 3-1 and 3-2 showing respective top and side views of the stepped-waveguide structure. The origin is placed in the cross-sectional center of the waveguide for mathematical convenience. Regions A $(z < 0)$ and B $(z > d_N)$ are air-filled waveguide sections having width a and height b. The reduced-aperture sample holder attached between regions A and B consists, in general, of a multi-

layered material stack. The sample holder is assumed to have a reduced width t symmetrically centered on the origin, but no reduction in height. The thickness of each layer in the sample region must comprise the total sample holder thickness

$$d_N = \sum_{i=1}^{N} \ell_i \qquad (3.2)$$

3.1.2 Mode Orthogonality.

The disruption in the waveguide-wall surface currents experienced at the waveguide to sample holder junctions will cause the excitation of higher-order modes. Examining (2-27), the transverse fields of the TE_{10} mode are readily seen to be y-invariant and even about the center width of the waveguide $(x = 0)$. Thus, since the aperture of the sample holder is reduced only in width and centered about $x = 0$, all higher-order excited modes will also be y-invariant and even about the waveguide width [9].

Considering only this limited set of possible higher-order mode shapes, the types of higher-order excited modes is significantly decreased. Although not specifically shown here, all TM modes are y-dependent and can thus be immediately discounted [8]. In addition, y-invariance of TE modes implies

$$n = 0 \quad \Rightarrow \quad k_y = 0 \quad \Rightarrow \quad \begin{matrix} e_x = 0 \\ h_y = 0 \end{matrix} \qquad (3.3)$$

which permits only TE_{m0} modes with the field equations

$$
\begin{aligned}
e_y &= -\frac{j\omega\mu}{k_c^2} A_{mn} k_x \sin\{k_x (x + \tfrac{a}{2})\} \\
h_x &= -\frac{e_y}{Z_{TE}}
\end{aligned}
\qquad (3.4)
$$

Then, using a trigonometric identity, the following simplification can be made

$$\sin\left\{k_x\left(x + \tfrac{a}{2}\right)\right\} = \begin{cases} (-1)^{\frac{m-1}{2}}\cos k_x x & , \quad m = 1,3,5,\dots \\ (-1)^{\frac{m}{2}}\sin k_x x & , \quad m = 2,4,6,\dots \end{cases} \tag{3.5}$$

Finally, the even requirement about $x = 0$ leaves only

$$\left.\begin{aligned} e_y &= -(-1)^{\frac{m-1}{2}}\frac{j\omega\mu}{k_c^2}A_{mn}k_x\cos k_x x = \tilde{A}_{mn}\cos k_x x \\ h_x &= -\frac{e_y}{Z_{TE}} = -\frac{e_y}{Z} \end{aligned}\right\} \quad m = 1,3,5,\dots \tag{3.6}$$

where $\tilde{A}_{mn}$ has been introduced to consolidate the constants, and the subscript on the wave impedance has been suppressed since only TE modes are possible.

Note that the physical insight leading to consideration of only this limited set of higher-order modes can be rigorously proven through mode orthogonality. That is, integrating the dot product of the transverse fields of the TE_{10} mode with any other mode over the cross-section of the sample holder aperture will yield zero. For example, consider integration over the sample holder aperture of the dot product of the electric fields of the TE_{10} mode with the TE_{m0} modes for even values of m:

$$\int_{-b/2}^{b/2}\int_{-t/2}^{t/2}\vec{e}_{TE_{10}}\cdot\vec{e}_{TE_{m0}}\,dx\,dy \quad, \quad m = 2,4,6\dots \tag{3.7}$$

Dropping the constants and ignoring integration over y (since all TE_{m0} modes are y-invariant) leads to

$$\int_{-t/2}^{t/2}\cos\frac{\pi x}{a}\sin\frac{m\pi x}{a}\,dx = 0 \quad, \quad m = 2,4,6\dots \tag{3.8}$$

3-4

which is readily identified as the integration of an odd function over symmetric limits yielding zero. Similarly, mode orthogonality can be used to disregard all TE_{mn} ($n \neq 0$) and TM modes. Thus, the only modes that will couple into the sample holder region will be TE_{m0} modes for odd values of m.

3.1.3 Field Expansions in Waveguide Regions.

The transverse fields in the waveguide regions are given by the following expansions

$$
\left. \begin{aligned}
\vec{E}_t^A &= a_1^+ \vec{e}_1 e^{-\gamma_1 z} + \sum_{m=1}^{M} a_m^- \vec{e}_m e^{\gamma_m z} \\
\vec{H}_t^A &= a_1^+ \vec{h}_1 e^{-\gamma_1 z} - \sum_{m=1}^{M} a_m^- \vec{h}_m e^{\gamma_m z}
\end{aligned} \right\} \dots z < 0 \tag{3.9}
$$

$$
\left. \begin{aligned}
\vec{E}_t^B &= \sum_{m=1}^{M} b_m^+ \vec{e}_m e^{-\gamma_m (z - d_N)} \\
\vec{H}_t^B &= \sum_{m=1}^{N} b_m^+ \vec{h}_m e^{-\gamma_m (z - d_N)}
\end{aligned} \right\} \dots z > d_N \tag{3.10}
$$

where a_1^+ represents the complex amplitude of the incident TE_{10} mode traveling in the positive z-direction, a_m^- represents the complex amplitude of the TE_{m0} mode reflected from the waveguide to sample holder junction at $z = 0$, b_m^+ represents the complex amplitude of the TE_{m0} mode transmitted through the sample region at $z = d_N$, and the negative sign in the $\vec{H}_t^A$ equation represents the polarization rotation upon reflection, which is consistent with the direction of power transport for the reflected wave. In addition, the following indexing convention has been adopted

$$\left.\begin{aligned}
\vec{e}_m &= \hat{y}\cos k_{xm}x \quad , \quad k_{xm} = (2m-1)\frac{\pi}{a} \\
\vec{h}_m &= \frac{\hat{z}\times\vec{e}_m}{Z_m} \quad , \quad Z_m = \frac{j\omega\mu_o}{\gamma_m} \quad , \quad \gamma_m = \sqrt{k_{xm}^2 - k_o^2}
\end{aligned}\right\} \quad m = 1, 2, ..., M \qquad (3.11)$$

where $k_o = \omega/c$ with $c = 1/\sqrt{\varepsilon_o\mu_o}$ as the speed of light in a vacuum.

While an infinite number of higher-order modes are actually excited at the waveguide to sample holder junction, the total number of modes M that must be considered for a given convergence threshold is dependent on the degree of reduction to the sample holder's aperture. Analogous to Fourier Transform theory, where a narrow pulse in the time domain translates to high-frequency components in the frequency domain, larger disruptions to the waveguide-wall surface currents will require more higher-order modes to accurately represent the discontinuity. For example, in an ideal sample holder that matches the dimensions of the waveguide, only the dominant TE$_{10}$ mode need be considered. However, as the width reduction increases, there is an appreciable amount of energy shifted to successive higher-order modes. Thus, as the sample holder aperture decreases, more higher-order modes are necessary to extract the correct material parameters.

3.1.4 Field Expansions in Sample Region.

Modeling the sample holder as a reduced-aperture multi-layer environment has two important advantages. First, it allows for an extra degree-of-freedom in the manufacturing process by not requiring the test sample to completely fill the sample holder thickness. In addition, for very low frequency applications where waveguide dimensions become very large, a rigid dielectric sandwich can be used to support thin, flimsy test samples. However, it is assumed that only one layer in the sample region has

unknown material properties. Thus, in the case of a dielectric sandwich, each dielectric support would have to be measured separately from the test sample.

The transverse field equations in the ith layer of the sample holder region are given by

$$\left. \begin{aligned} \vec{E}_t^{s,i} &= \sum_{m=1}^{M} s_{m,i}^{+} \vec{e}_m^{s} e^{-\gamma_m^{s,i}(z-d_i)} + \sum_{m=1}^{M} s_{m,i}^{-} \vec{e}_m^{s} e^{\gamma_m^{s,i}(z-d_i)} \\ \vec{H}_t^{s,i} &= \sum_{m=1}^{M} s_{m,i}^{+} \vec{h}_m^{s,i} e^{-\gamma_m^{s,i}(z-d_i)} - \sum_{m=1}^{M} s_{m,i}^{-} \vec{h}_m^{s,i} e^{\gamma_m^{s,i}(z-d_i)} \end{aligned} \right\} \quad d_{i-1} < z < d_i \qquad (3.12)$$

where the superscript s is used to indicate the sample holder region, and the distance to each reference plane is determined by

$$d_i = \sum_{k=1}^{i} \ell_k \qquad (3.13)$$

An indexing convention similar to (3.11) has also been adopted:

$$\left. \begin{aligned} \vec{e}_m^{s} &= \hat{y} \cos k_{xm}^{s} x \quad, \quad k_{xm}^{s} = (2m-1) \frac{\pi}{t} \\ \vec{h}_m^{s,i} &= \frac{\hat{z} \times \vec{e}_m^{s}}{Z_m^{s,i}} \quad, \quad Z_m^{s,i} = \frac{j\omega\mu_i}{\gamma_m^{s,i}} \quad, \quad \gamma_m^{s,i} = \sqrt{k_{xm}^{s2} - k_i^2} \end{aligned} \right\} \quad m = 1,2,...,M \qquad (3.14)$$

where the complex relative permittivity and permeability of each layer determine the wave number of the corresponding medium $k_i = \frac{\omega}{c} \sqrt{\varepsilon_{r,i}\mu_{r,i}}$.

3.2 Satisfying Boundary Conditions

The second step of the modal analysis process is to satisfy boundary conditions across each interface. Enforcing continuity of the tangential fields across the waveguide to sample holder interfaces at $z = 0, d_N$ leads to

$$a_1^+ \vec{e}_1 + \sum_{m=1}^{M} a_m^- \vec{e}_m = \begin{cases} \displaystyle\sum_{m=1}^{M} s_{m,1}^+ \vec{e}_m^s e^{\gamma_m^{s,1} d_1} + \sum_{m=1}^{M} s_{m,1}^- \vec{e}_m^s e^{-\gamma_m^{s,1} d_1} & \cdots \ |x| < t/2 \\[2mm] 0 & \cdots \ -a/2 < x < -t/2 \ , \ t/2 < x < a/2 \end{cases} \tag{3.15}$$

$$a_1^+ \vec{h}_1 - \sum_{m=1}^{M} a_m^- \vec{h}_m = \sum_{m=1}^{M} s_{m,1}^+ \vec{h}_m^{s,1} e^{\gamma_m^{s,1} d_1} - \sum_{m=1}^{M} s_{m,1}^- \vec{h}_m^{s,1} e^{-\gamma_m^{s,1} d_1} \quad \cdots \ |x| < t/2 \tag{3.16}$$

$$\sum_{m=1}^{M} b_m^+ \vec{e}_m = \begin{cases} \displaystyle\sum_{m=1}^{M} s_{m,N}^+ \vec{e}_m^s + \sum_{m=1}^{M} s_{m,N}^- \vec{e}_m^s & \cdots \ |x| < t/2 \\[2mm] 0 & \cdots \ -a/2 < x < -t/2 \ , \ t/2 < x < a/2 \end{cases} \tag{3.17}$$

$$\sum_{m=1}^{M} b_m^+ \vec{h}_m = \sum_{m=1}^{M} s_{m,N}^+ \vec{h}_m^{s,N} - \sum_{m=1}^{M} s_{m,N}^- \vec{h}_m^{s,N} \quad \cdots \ |x| < t/2 \tag{3.18}$$

Note that as a consequence of the uniqueness theorem, it is only necessary to satisfy the magnetic field boundary condition in the region $|x| < t/2$ since the tangential electric field boundary condition is known absolutely (i.e. $\vec{E}_{tang} = 0$) in the regions $-a/2 < x < -t/2$ and $t/2 < x < a/2$ at $z = 0, d_N$.

Enforcement of the boundary conditions across the material interfaces in the sample holder region is inherently built into the wave transmission analysis outlined in the previous chapter. In addition, as a result of the mode orthogonality that exists within the sample holder region, the amplitude coefficients in the first region are related to those in layer N by

$$\begin{aligned} \begin{bmatrix} s_{m,1}^+ \\ s_{m,1}^- \end{bmatrix} &= \prod_{i=2}^{N} \frac{1}{\tau_m^{s,i}} \begin{bmatrix} e^{\gamma_m^{s,i} \ell_i} & \Gamma_m^{s,i} e^{-\gamma_m^{s,i} \ell_i} \\ \Gamma_m^{s,i} e^{\gamma_m^{s,i} \ell_i} & e^{-\gamma_m^{s,i} \ell_i} \end{bmatrix} \begin{bmatrix} s_{m,N}^+ \\ s_{m,N}^- \end{bmatrix} \\[2mm] &= \begin{bmatrix} A_{11}^m & A_{12}^m \\ A_{21}^m & A_{22}^m \end{bmatrix} \begin{bmatrix} s_{m,N}^+ \\ s_{m,N}^- \end{bmatrix} \end{aligned} \tag{3.19}$$

where now the c_i, b_i of (2.35) are replaced by $s_{m,i}^+, s_{m,i}^-$ and

$$\Gamma_m^{s,i} = \frac{Z_m^{s,i} - Z_m^{s,i-1}}{Z_m^{s,i} + Z_m^{s,i-1}} \quad , \quad \tau_m^{s,i} = 1 + \Gamma_m^{s,i} \qquad (3.20)$$

The index m expresses that the A-parameters will be different for each mode that is excited at the waveguide to sample holder junctions. However, since the height and width remain constant throughout the entire sample holder, each mode will couple independently though each layer, as mentioned in the mode orthogonality discussion above. For example, if the TE_{30} mode is present in layer one, then it will couple completely into the TE_{30} mode in layers two, three, four, etc., but will not affect the TE_{10} or TE_{50} modes in those layers.

3.3 Testing with Integral Operators

Before implementing the last step of the modal-analysis process, it is beneficial to review the results of the previous boundary condition enforcement section. If $s_{m,1}^+, s_{m,1}^-$ from (3.19) are substituted into (3.15)-(3.16) and then each remaining coefficient in (3.15)-(3.18) is divided by a_1^+, there will be 4 linearly independent equations with $4M$ unknown ratios (having numerators $a_m^-, s_{m,N}^+, s_{m,N}^-, b_m^+$). However, to solve for these unknown coefficient ratios, it is necessary to have $4M$ linearly independent equations with $4M$ unknowns. Similar to a *method of moments* technique [10], application of properly chosen inner product testing operators will generate the required $4M$ equations.

Consider the testing operators

$$\int_{-b/2}^{b/2} \int_{-a/2}^{a/2} \vec{e}_n \cdot \{\ \} \, dx dy \quad , \quad n = 1, 2, \dots M \qquad (3.21)$$

$$Z_n^s \int_{-b/2}^{b/2} \int_{-t/2}^{t/2} \vec{h}_n^s \cdot \{ \ \} \, dx dy \quad , \quad n = 1, 2, \dots M \tag{3.22}$$

where the uniqueness theorem is again used to limit the magnetic field intensity operator

to $-t/2 \le x \le t/2$ and Z_n^s multiplies the inner product to express the fact the operator is

not linked to a specific material layer in the sample holder region. Applying (3.21) to

(3.15),(3.17) and (3.22) to (3.16),(3.18) produces

$$a_1^+ \overbrace{\int_0^{a/2} \vec{e}_n \cdot \vec{e}_1 dx}^{C_{n1}} + \sum_{m=1}^{M} a_m^- \overbrace{\int_0^{a/2} \vec{e}_n \cdot \vec{e}_m dx}^{C_{nm}} = \sum_{m=1}^{M} s_{m,1}^+ e^{\gamma_m^{s,1} d_1} \overbrace{\int_0^{t/2} \vec{e}_n \cdot \vec{e}_m^s dx}^{D_{nm}} + \sum_{m=1}^{M} s_{m,1}^- e^{-\gamma_m^{s,1} d_1} \overbrace{\int_0^{t/2} \vec{e}_n \cdot \vec{e}_m^s dx}^{D_{nm}} \tag{3.23}$$

$$a_1^+ Z_n^s \overbrace{\int_0^{t/2} \vec{h}_n^s \cdot \vec{h}_1 dx}^{F_{n1}} - \sum_{m=1}^{M} a_m^- Z_n^s \overbrace{\int_0^{t/2} \vec{h}_n^s \cdot \vec{h}_m dx}^{F_{nm}}$$

$$= \sum_{m=1}^{M} s_{m,1}^+ e^{\gamma_m^{s,1} d_1} Z_n^s \overbrace{\int_0^{t/2} \vec{h}_n^s \cdot \vec{h}_m^{s,1} dx}^{P_{nm}} - \sum_{m=1}^{M} s_{m,1}^- e^{-\gamma_m^{s,1} d_1} Z_n^s \overbrace{\int_0^{t/2} \vec{h}_n^s \cdot \vec{h}_m^{s,1} dx}^{P_{nm}} \tag{3.24}$$

$$\sum_{m=1}^{M} b_m^+ \overbrace{\int_0^{a/2} \vec{e}_n \cdot \vec{e}_m dx}^{C_{nm}} = \sum_{m=1}^{M} s_{m,N}^+ \overbrace{\int_0^{t/2} \vec{e}_n \cdot \vec{e}_m^s dx}^{D_{nm}} + \sum_{m=1}^{M} s_{m,N}^- \overbrace{\int_0^{t/2} \vec{e}_n \cdot \vec{e}_m^s dx}^{D_{nm}} \tag{3.25}$$

$$\sum_{m=1}^{M} b_m^+ Z_n^s \overbrace{\int_0^{t/2} \vec{h}_n^s \cdot \vec{h}_m dx}^{F_{nm}} = \sum_{m=1}^{M} s_{m,N}^+ Z_n^s \overbrace{\int_0^{t/2} \vec{h}_n^s \cdot \vec{h}_m^{s,N} dx}^{Q_{nm}} - \sum_{m=1}^{M} s_{m,N}^- Z_n^s \overbrace{\int_0^{t/2} \vec{h}_n^s \cdot \vec{h}_m^{s,N} dx}^{Q_{nm}} \tag{3.26}$$

where the integration over y cancels out due to the y-invariance of the problem and

evenness in x was also used to limit the integration to only half the waveguide or sample

holder width. The resulting integrals have the closed-form solutions

$$C_{nm} = \int_0^{a/2} \vec{e}_n \cdot \vec{e}_m dx = \begin{cases} \dfrac{a}{4} & \dots \ m = n \\ 0 & \dots \ m \ne n \end{cases} \tag{3.27}$$

$$D_{nm} = \int_0^{t/2} \vec{e}_n \cdot \vec{e}_m^s \, dx = \begin{cases} \dfrac{t}{4} & \cdots \quad k_{xm}^s = k_{xn} \\[2ex] (-1)^m \dfrac{k_{xm}^s \cos{k_{xn}t/2}}{k_{xn}^2 - k_{xm}^{s2}} & \cdots \quad k_{xm}^s \neq k_{xn} \end{cases} \tag{3.28}$$

$$F_{nm} = Z_n^s \int_0^{t/2} \vec{h}_n^s \cdot \vec{h}_m \, dx = \begin{cases} \dfrac{t}{4Z_m} & \cdots \quad k_{xm} = k_{xn}^s \\[2ex] (-1)^n \dfrac{k_{xn}^s}{Z_m} \dfrac{\cos{k_{xm}t/2}}{k_{xm}^2 - k_{xn}^{s2}} & \cdots \quad k_{xm} \neq k_{xn}^s \end{cases} \tag{3.29}$$

$$P_{nm} = Z_n^s \int_0^{t/2} \vec{h}_n^s \cdot \vec{h}_m^{s,1} \, dx = \begin{cases} \dfrac{t}{4Z_m^{s,1}} & \cdots \quad m = n \\[2ex] 0 & \cdots \quad m \neq n \end{cases} \tag{3.30}$$

$$Q_{nm} = Z_n^s \int_0^{t/2} \vec{h}_n^s \cdot \vec{h}_m^{s,N} \, dx = \begin{cases} \dfrac{t}{4Z_m^{s,N}} & \cdots \quad m = n \\[2ex] 0 & \cdots \quad m \neq n \end{cases} \tag{3.31}$$

where the details are located in Appendix A for the interested reader.

Substitution of $s_{m,1}^+, s_{m,1}^-$ from (3.19) into (3.23),(3.24) and dividing the remaining

coefficients in (3.23)-(3.26) by a_1^+ gives

$$C_{n1} + \sum_{m=1}^{M} R_m C_{nm} = \sum_{m=1}^{M} T_m \overbrace{D_{nm}\left(A_{11}^m e^{\gamma_m^{s,1}d_1} + A_{21}^m e^{-\gamma_m^{s,1}d_1}\right)}^{U_{nm}} + \sum_{m=1}^{M} r_m \overbrace{D_{nm}\left(A_{12}^m e^{\gamma_m^{s,1}d_1} + A_{22}^m e^{-\gamma_m^{s,1}d_1}\right)}^{V_{nm}} \tag{3.32}$$

$$F_{n1} - \sum_{m=1}^{M} R_m F_{nm} = \sum_{m=1}^{M} T_m \overbrace{P_{nm}\left(A_{11}^m e^{\gamma_m^{s,1}d_1} - A_{21}^m e^{-\gamma_m^{s,1}d_1}\right)}^{W_{nm}} - \sum_{m=1}^{M} r_m \overbrace{P_{nm}\left(-A_{12}^m e^{\gamma_m^{s,1}d_1} + A_{22}^m e^{-\gamma_m^{s,1}d_1}\right)}^{Y_{nm}} \tag{3.33}$$

$$\sum_{m=1}^{M} R_m C_{nm} = \sum_{m=1}^{M} T_m D_{nm} + \sum_{m=1}^{M} r_m D_{nm} \tag{3.34}$$

$$\sum_{m=1}^{M} R_m F_{nm} = \sum_{m=1}^{M} T_m Q_{nm} - \sum_{m=1}^{M} r_m Q_{nm} \tag{3.35}$$

with the coefficient ratios

$$R_m = \frac{a_m^-}{a_1^+} \quad, \quad T_m = \frac{s_{m,N}^+}{a_1^+} \quad, \quad r_m = \frac{s_{m,N}^-}{a_1^+} \quad, \quad t_m = \frac{b_m^+}{a_1^+} \tag{3.36}$$

One final rearrangement leads to the desired result of $4M$ linearly independent equations

with $4M$ unknowns:

$$\left. \begin{aligned} \sum_{m=1}^{M} C_{nm} R_m - \sum_{m=1}^{M} U_{nm} T_m - \sum_{m=1}^{M} V_{nm} r_m &= -C_{n1} \\ \sum_{m=1}^{M} F_{nm} R_m + \sum_{m=1}^{M} W_{nm} T_m - \sum_{m=1}^{M} Y_{nm} r_m &= F_{n1} \\ \sum_{m=1}^{M} D_{nm} T_m + \sum_{m=1}^{M} D_{nm} r_m - \sum_{m=1}^{M} C_{nm} t_m &= 0 \\ \sum_{m=1}^{M} Q_{nm} T_m - \sum_{m=1}^{M} Q_{nm} r_m - \sum_{m=1}^{M} F_{nm} t_m &= 0 \end{aligned} \right\} \quad n = 1,2,\ldots,M \tag{3.37}$$

which can then be written in the partitioned-matrix form

$$\begin{bmatrix} C & -U & -V & 0 \\ F & W & -Y & 0 \\ 0 & D & D & -C \\ 0 & Q & -Q & -F \end{bmatrix} \begin{bmatrix} R \\ T \\ r \\ t \end{bmatrix} = \begin{bmatrix} x_1 \\ x_2 \\ 0 \\ 0 \end{bmatrix} \tag{3.38}$$

where C, U, V, F, W, Y, D, Q are $M \times M$ sub-matrices and x_1, x_2 are the column vectors

given as

$$x_1 = -\begin{bmatrix} C_{11} \\ C_{21} \\ \vdots \\ C_{M1} \end{bmatrix} \quad, \quad x_2 = \begin{bmatrix} F_{11} \\ F_{21} \\ \vdots \\ F_{M1} \end{bmatrix} \tag{3.39}$$

3.4 Material Parameter Extraction.

The matrix equation of (3.38) is readily solved for the coefficient ratios of (3.36) by Gaussian elimination. Since the waveguide will be setup for dominant TE_{10} mode operation, all the higher-order reflected and transmitted modes excited by the reduced-width sample holder will evanesce before returning to the network analyzer. That is, while the higher-order modes will influence the TE_{10} propagating mode amplitudes, only the reflected and transmitted components of the TE_{10} mode will arrive at the detector elements. Thus, the theoretical coefficient ratios of primary interest are

$$R_1 = S_{11}^{thy}(\omega, \varepsilon, \mu) \quad , \quad t_1 = S_{21}^{thy}(\omega, \varepsilon, \mu) \tag{3.40}$$

To extract the material parameters at each frequency, an iterative optimization algorithm is used to find the complex permittivity and permeability that best match the theoretically calculated to the experimentally measured S-parameter as described by (3.1). For a homogenous material, a nonlinear least-squares algorithm utilizing all four S-parameters from the forward and reverse traveling waves perhaps offers the best method to filter out the noise inherent in the system. However, a complex 2-dimensional Newton's root-searching algorithm can be used to solve the forward and reverse problems separately and provide insight into possible inhomogeneities or gross measurement errors.

Note that the material parameter extractions presented in this thesis were performed by Matlab's® nonlinear least-squares algorithm. As a precaution to the reader, this algorithm requires all variables to be real. Thus, it is necessary to break the permittivity and permeability into their respective real and imaginary parts.

3.5 Summary

A three step modal analysis technique was developed to accommodate the higher-order modes excited by the stepped junction between the waveguide feeds and the multi-layered reduced-width sample holder region. The problem was formulated into a partitioned-matrix form to solve for the theoretical S-parameters for a guess at the constitutive material parameters. Finally, two optimization algorithms for extracting the test sample's material parameters from the experimental S-parameters were suggested.

4. Results and Error Analysis

To verify the modal-analysis technique developed in Chapter 3, several materials were measured in the S-band frequency range, $2.6 - 3.95 \text{ GHz}$. While the technique is intended for low-frequency applications with large test samples, the smaller S-band waveguide samples were adequate, and much less expensive, for a proof-of-concept demonstration. In this chapter, experimental results will be shown for acrylic, magnetic radar absorbing material (MRAM), and electric radar absorbing material (ERAM). In addition, a brief study of the number of higher-order modes required for material parameter convergence for different sample holder aperture reductions will be presented.

When conducting any experimental procedure, there are many possible error sources. Assuming a good calibration, properly machined sample holders with precision alignment pins, and quality test samples with uniform thickness and material composition, user error can still lead to inaccuracies in the constitutive parameter extractions when performing these waveguide measurements. A differential error analysis will be presented to develop error bounds related to test sample thickness and placement measurement errors.

4.1 Experimental Setup

The experimental setup is as shown in Figure 4-1 with a WR284 waveguide (where WR stands for "waveguide rectangular" and 284 refers to the inner waveguide width $a = 2.84 \text{ inches}$) connected to a HP8510C Vector Network Analyzer via coaxial

cables. The reduced-aperture sample holder is mounted to the waveguide with precision

alignment pins to minimize the discontinuities across the interfaces. Also, great care was

taken to clean all cabling junctions with isopropyl alcohol to ensure proper electrical

contacts. Finally, a full two-port *thru, reflect, line* (TRL) calibration procedure was used

to set the calibration planes immediately before and immediately after the sample holder

(at $z = 0, d_N$ with reference to Figure 3-1) [9].

The three sample holders used to verify the modal-analysis technique are shown

in Figure 4-2. The sample holder on the left has the same dimensions as the waveguide

feeds and was used to set the baselines, since only the dominant TE_{10} mode was required

for material parameter extraction. The sample holders in the middle and on the right of

Figure 4-2 have reduced width, but no reduction in height. It will be shown that

comparable results can be obtained using the reduced-width sample holders by

accounting for the higher-order modes that are excited at the waveguide feed to sample

holder junctions.

Even before measuring any test samples there were a few additional steps taken to

validate the experimental setup. First, after performing the calibration, the shorting

standard (brass plate) used in the *reflect* portion of the TRL calibration procedure was

measured again to ensure that $S_{11,22}^{exp} \approx -1 - j0$ and $S_{21,12}^{exp} \approx 0 - j0$. Also, an extraction was

performed on the S-parameters measured from the empty sample holders to ensure a free

space baseline for the system.
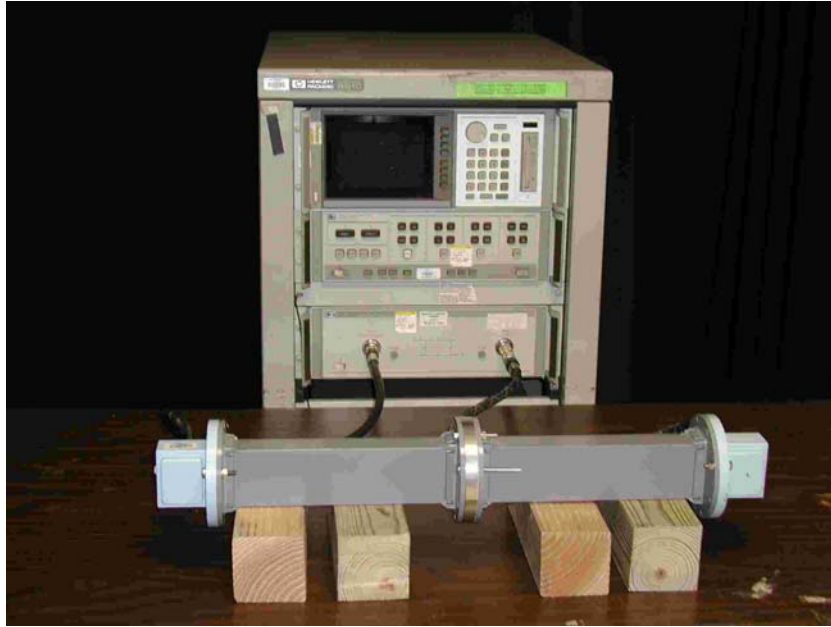
Figure 4-1. Experimental setup showing a WR284 waveguide connected to an HP8510C Vector Network Analyzer with coaxial cables. The reduced-aperture sample holder is mounted between the waveguide feeds with precision alignment pins.

Figure 4-2. S-band waveguide sample holders. On the left is the full-aperture sample holder having the same dimensions as the waveguide feeds, while the ones in the middle and on the right have a reduced width, but no reduction in height.

4.2 Error Analysis

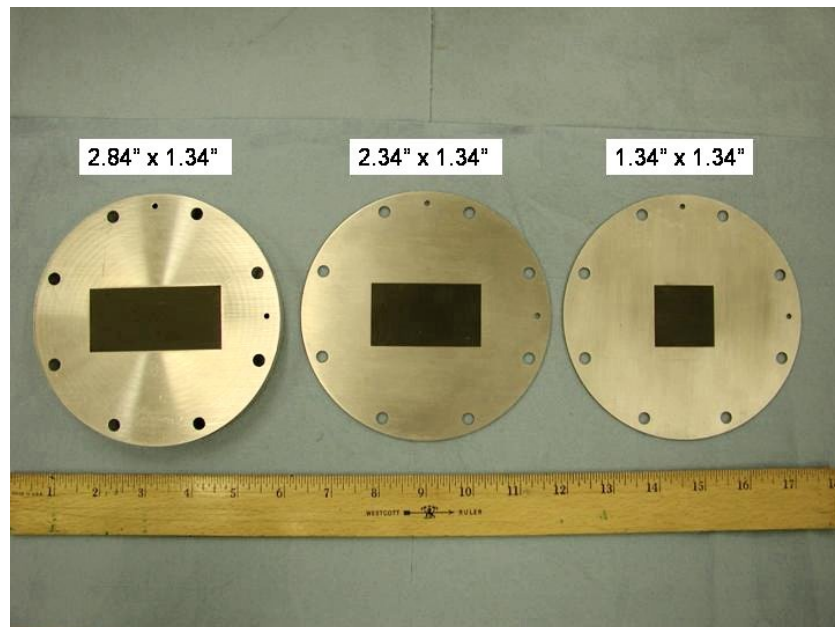Before proceeding with the differential error analysis development, it is necessary to first review the big picture goal of the modal-analysis technique derivation of the previous chapter. The complex relative permittivity and permeability of the test sample will be determined using an iterative nonlinear least-squares optimization algorithm that seeks to match the theoretically calculated to the experimentally measured S-parameters:

$$\min\left\{\sum_i \left[S_i^{thy}(\omega,\varepsilon,\mu) - S_i^{exp}(\omega) \right]^2\right\} \tag{3.1}$$

where $i = 11, 21, 22, 12$. Thus, uncertainties in the experimental S-parameters will clearly lead to different ε, μ values that satisfy (3.1). In addition, given "perfect" experimental S-parameters with no added random noise or drift, there are obviously many other possible error contributions that will lead to extraction inaccuracies. Uncertainties in sample holder dimensions (width, height, length – t, b, d_N), alignment errors causing excitation of undesired higher-order modes, and absorption due to the imperfectly conducting sample holder walls are just a few possible error sources. However, carefully machined sample holders with precision alignment pins lead to very good empty-aperture baselines, and experience has shown that user error in measuring test sample thickness and placement within the sample holder are two of the most sensitive and difficult to control parameters.

To account for the test sample thickness and placement measurement errors, a differential error analysis was performed. With the estimated permittivity written as a function of thickness ℓ and placement p,

$$\varepsilon = \varepsilon'(\ell, p) - j\varepsilon''(\ell, p) \tag{4.1}$$

the Taylor series expansion of the real part around the point (ℓ_o, p_o) is given as

$$\varepsilon'(\ell_o + \Delta\ell, p_o + \Delta p) = \varepsilon'(\ell_o, p_o) + \frac{\partial\varepsilon'(\ell_o, p_o)}{\partial\ell}\Delta\ell + \frac{\partial\varepsilon'(\ell_o, p_o)}{\partial p}\Delta p + \dots \tag{4.2}$$

where $\Delta\ell$ is the uncertainty in the measured thickness ℓ_o, and Δp is the uncertainty in placement at the location p_o. For relatively small $\Delta\ell$ and Δp, the higher-order terms of the Taylor series expansion can be neglected and the change in the real permittivity can be represented as

$$\Delta\varepsilon'_{exact} = \varepsilon'(\ell_o + \Delta\ell, p_o + \Delta p) - \varepsilon'(\ell_o, p_o) \approx \frac{\partial\varepsilon'(\ell_o, p_o)}{\partial\ell}\Delta\ell + \frac{\partial\varepsilon'(\ell_o, p_o)}{\partial p}\Delta p = \Delta\varepsilon'_{approx} \tag{4.3}$$

Next, the partial derivatives can be approximated (again assuming small $\Delta\ell$ and Δp) by

$$\Delta\varepsilon'_\ell = \frac{\partial\varepsilon'(\ell_o, p_o)}{\partial\ell}\Delta\ell \approx \frac{\varepsilon'(\ell_o + \Delta\ell, p_o) - \varepsilon'(\ell_o, p_o)}{\Delta\ell}\Delta\ell = \varepsilon'(\ell_o + \Delta\ell, p_o) - \varepsilon'(\ell_o, p_o) \tag{4.4}$$

$$\Delta\varepsilon'_p = \frac{\partial\varepsilon'(\ell_o, p_o)}{\partial p}\Delta p \approx \frac{\varepsilon'(\ell_o, p_o + \Delta p) - \varepsilon'(\ell_o, p_o)}{\Delta p}\Delta p = \varepsilon'(\ell_o, p_o + \Delta p) - \varepsilon'(\ell_o, p_o) \tag{4.5}$$

In general, $\Delta\ell$ and Δp can be positive or negative values. For small relative perturbations, the respective errors $\Delta\varepsilon'_\ell$ and $\Delta\varepsilon'_p$ will be symmetric about the unperturbed $\varepsilon'(\ell_o, p_o)$. However, for larger perturbations, the symmetry will start to break down and the errors generated by the positive and negative values must be computed separately to determine the worst-case contributions.

It should also be clear that independent material parameter extractions for the perturbations in the measured thickness and placement of the test sample can be

conducted and then combined to determine the overall error bounds related to those specific uncertainties. In combining the results, the triangle inequality is used to form an approximation of the worst-case errors in the real permittivity

$$\left| \Delta\varepsilon'_{approx} \right| = \left| \Delta\varepsilon' \right| = \left| \Delta\varepsilon'_{\ell} + \Delta\varepsilon'_{p} \right| \leq \left| \Delta\varepsilon'_{\ell} \right| + \left| \Delta\varepsilon'_{p} \right| \tag{4.6}$$

The triangle inequality is generally applied to vectors with the geometric interpretation that the sum of the lengths of any two sides of a triangle is always greater than the length of the remaining side. In this case, where $\Delta\varepsilon'_{\ell}, \Delta\varepsilon'_{p}$ are scalar quantities, the inequality is simply used to prevent cancellation between positive and negative error contributions.

It must be noted that often independent error contributions are added in quadrature [4] (i.e., $\left| \Delta\varepsilon' \right| = \sqrt{(\Delta\varepsilon'_{\ell})^2 + (\Delta\varepsilon'_{p})^2}$), but that assumes normally distributed errors where the sum of all deviations around the nominally measured values are negligible. In addition, the least-squares optimization algorithm tends to further exacerbate the problem, thus favoring the worst-case approach. Finally, the error analyses for the imaginary permittivity and real and imaginary permeability follow in a similar manner.

4.3 Acrylic

The acrylic measured for this thesis was a clear plexiglass-type material that exhibited almost pure dielectric characteristics with very little electric loss and no magnetic properties. In addition, due to its rigid structure, acrylic is easily machined into tightly fitting waveguide samples with almost uniform thickness. Because of these favorable qualities, acrylic was an ideal material to start the modal-analysis verification.

Having *a priori* knowledge of the dielectric nature of the test sample, a permittivity only extraction using all four S-parameters was conducted first on a full-size test sample to set the baseline relative dielectric constant at about 2.65 across the S-band frequency range. Note that the test sample was mounted flush toward the front surface of the full-aperture sample holder (facing terminal one of the network analyzer) to minimize the difficulty in measuring sample placement.

A second acrylic test sample was measured in the 2.34-inch reduced-width sample holder. Figure 4-3 shows that about 10 modes were required to converge to the full-aperture baseline. That is, the energies spread into higher-order modes must be accounted for to obtain accurate results. Note that error bounds related to uncertainty in test sample thickness or placement were not considered since the results were virtually identical to the full-aperture baseline.

Finally, a third acrylic test sample was measured in the 1.34-inch reduced-width sample holder. With a larger disruption in the waveguide wall surface currents, more modes were required for convergence to the full-aperture baseline. As shown in Figure 4-4, about 20 modes were required to obtain accurate results in the more tightly choked sample holder. Note that the imaginary permittivity graphs were not explicitly shown since they exhibited very low loss and added nothing additional to the discussion.
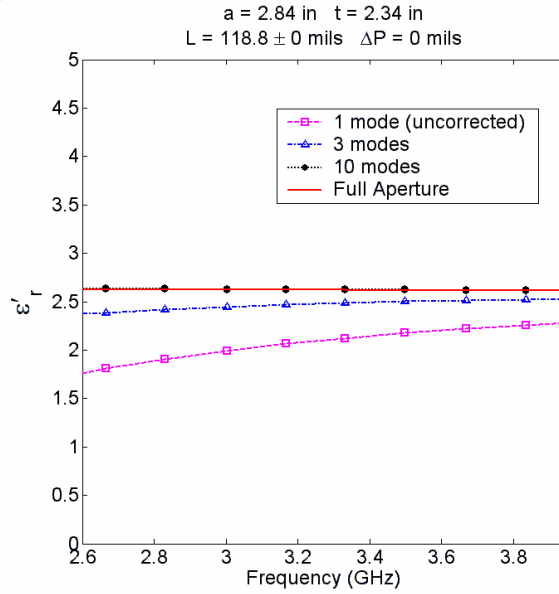
Figure 4-3. Real permittivity for acrylic test sample mounted flush toward port one in the 2.34-inch sample holder. About 10 modes are required for convergence to the full-aperture baseline. (Permittivity only extraction using least-squares algorithm on all four S-parameters.)
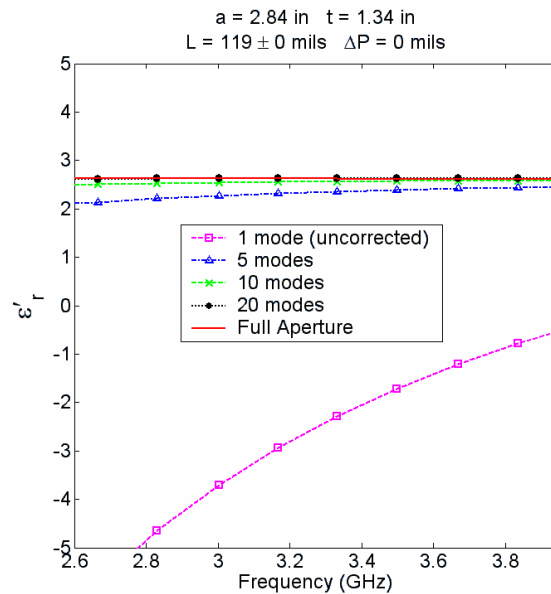

Figure 4-4. Real permittivity for acrylic test sample mounted flush toward port one in the 1.34-inch sample holder. About 20 modes are required for convergence to the full-aperture baseline. (Permittivity only extraction using least-squares algorithm on all four S-parameters.)

4.4 MRAM

Moving on to a more complicated extraction, three properly sized MRAM test samples were measured employing the same basic procedures used for the acrylic. In all cases, the samples were mounted flush to the front surfaces of the sample holders to minimize placement uncertainty. In addition, when using the reduced-width sample holders, the number of modes was increased until convergence was achieved. However, since the MRAM material was expected to exhibit magnetic properties, the nonlinear least-squares algorithm was setup for both a complex relative permittivity and permeability extraction.

The results for the MRAM measured in the 2.34-inch reduced-width sample holder are compared to the full-aperture baselines in Figure 4-5 and Figure 4-6. The permeability is seen to be nearly identical with the full-aperture baseline, and the minor difference in the real permittivity is readily explained by a 2-mil uncertainty in thickness and a 1-mil uncertainty in placement. The MRAM material used was manufactured with an adhesive on one side, which, when removed with sandpaper, led to slight fluctuations in thickness across the sample.

Similarly, Figure 4-7 and Figure 4-8 show the results for the MRAM measurement in the 1.34-inch sample holder. Again, the permittivity differences are mostly explained by the thickness and placement uncertainties. However, the error bars do not completely account for the 1.45% maximum discrepancy in the real permeability relative to its full-aperture baseline. This small discrepancy is mainly attributed to the grooves left by the sandpaper, but other possible errors due to uncertainty in the

experimental S-parameters and sample holder dimensions and alignment likely

contributed to the deviation from the full-aperture real permeability baseline. Better

results would most likely be attained with a test sample that was manufactured without an

adhesive, or if a less destructive method was used to remove the adhesive. In addition,

each test sample was cut separately from a large sheet. Improvements might be made if

the full-aperture test sample were measured, and then cut down for a measurement in the

 2.34-inch sample holder, and then cut down again for a measurement in the 1.34-inch

sample holder. By using portions of the original full-aperture test sample, errors due to

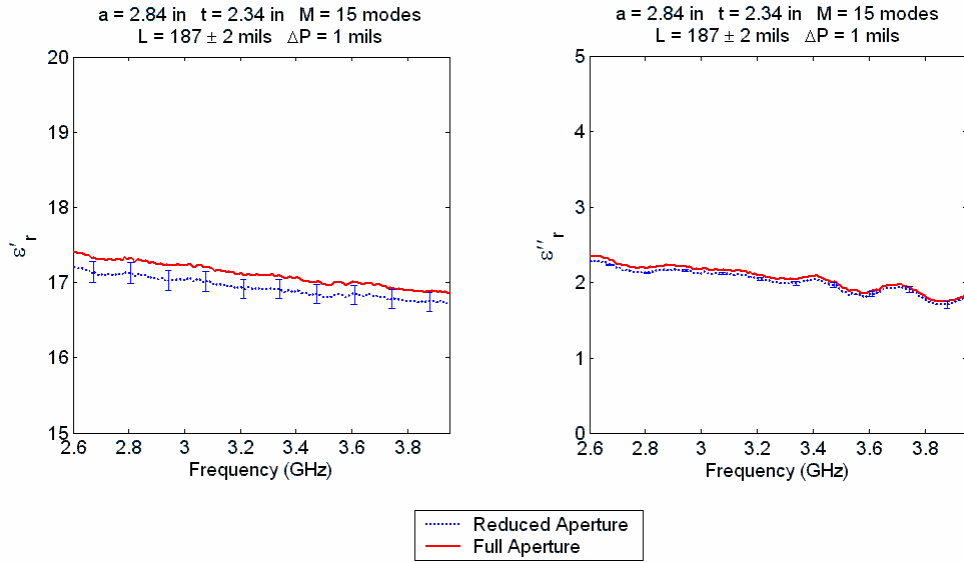fluctuations in material composition across the large sheets would be reduced.

Figure 4-5. Permittivity of MRAM test sample mounted flush toward port one in the
2.34-inch sample holder. Small difference in real part easily explained by uncertainty in
measured thickness and placement.
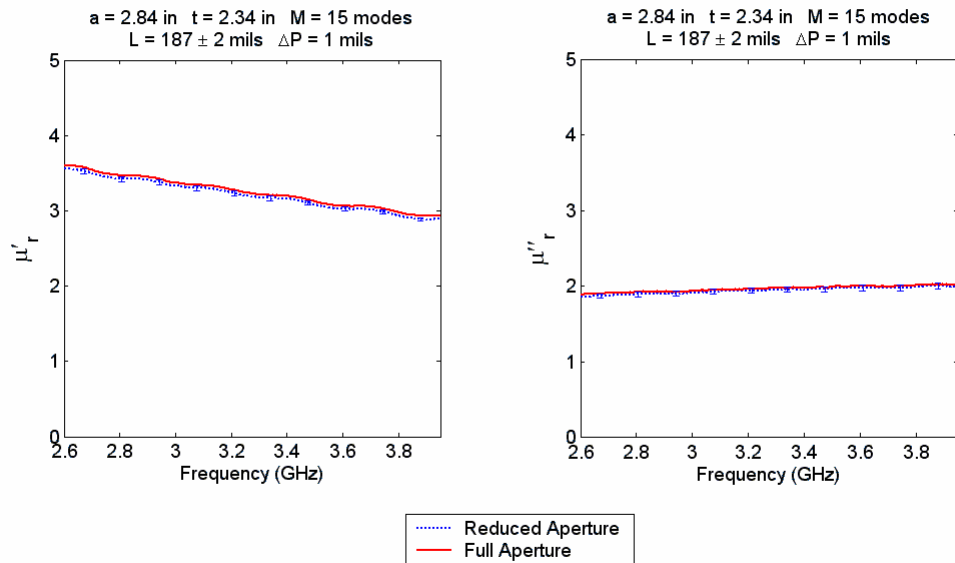
Figure 4-6. Permeability of MRAM test sample mounted flush toward port one in the
2.34-inch sample holder.
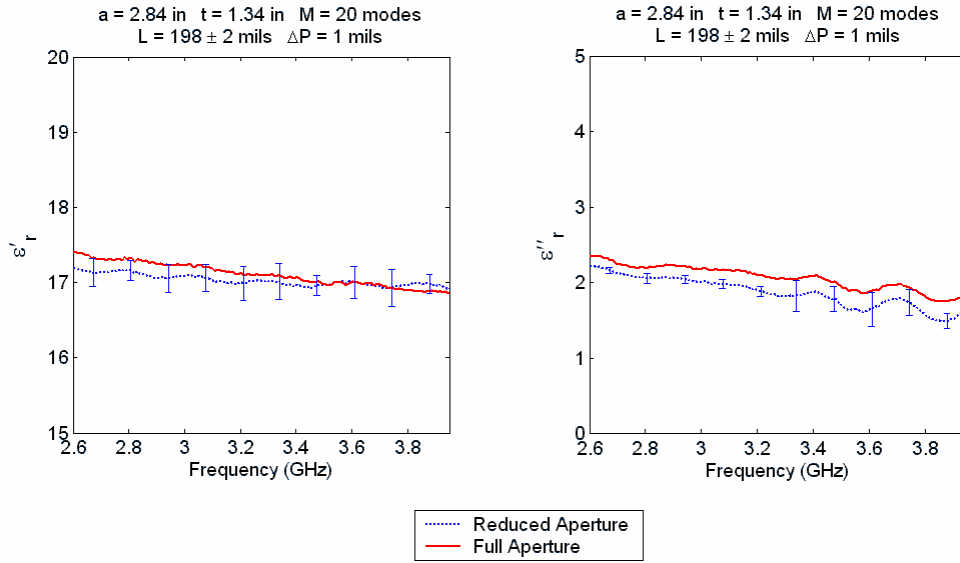
Figure 4-7. Permittivity of MRAM test sample mounted flush toward port one in the 1.34-inch sample holder. Thickness and placement uncertainty explain most of the difference relative to the full-aperture baseline.

Figure 4-8. Permeability of MRAM test sample mounted flush toward port one in the 1.34-inch sample holder. Maximum real permeability difference is 1.45% of full-aperture baseline without considering the thickness and placement uncertainties.
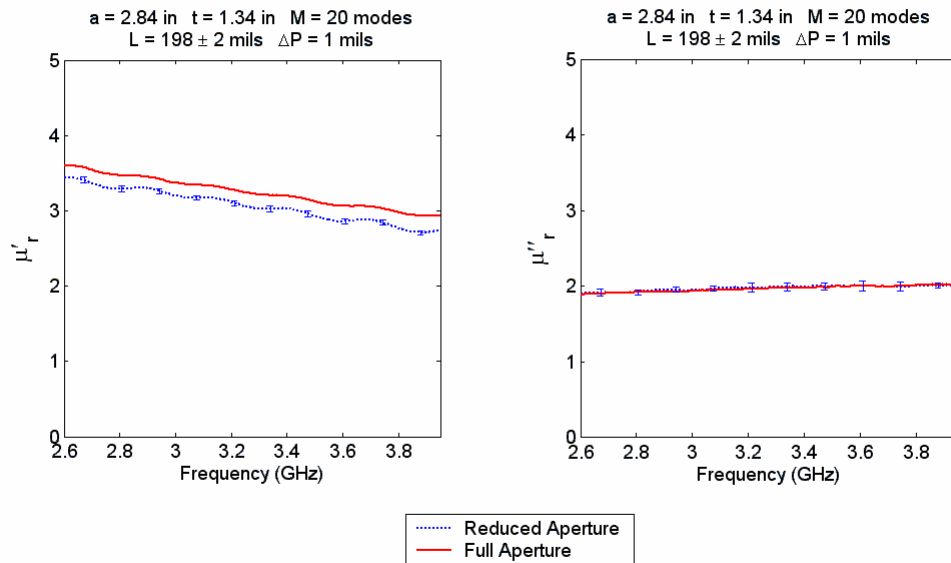
4.5 ERAM

The final material measured for this thesis was the ERAM, which consisted of a carbon-based foam from which it proved very difficult to cut precision test samples. Loose-fitting test samples led to energy leaking through the air gaps between the test sample and the sample holder walls. On the other hand, test samples that were cut too large caused compression of the foam also leading to inaccuracies. In addition, it was very difficult to accurately measure the thickness of the test samples since the foam was easily compressed by the inch micrometer.

Three separate attempts were made to measure ERAM. The results shown in Figure 4-9 and Figure 4-10 are representative of all three attempts. The error bars related to a 5-mil uncertainty in measured thickness and a 1-mil uncertainty in placement do not fully explain the discrepancies between the reduced-width test samples and the full-aperture baseline. Similar error bars added to the full-aperture baseline would still not completely account for the differences. Without taking the error bars into account, the real/imaginary permittivity of the test sample measured in the 2.34-inch sample holder is within 6.55/14.22% of the full-aperture baselines. Similarly, the real/imaginary permittivity of the ERAM measured in the 1.34-inch sample holder is within 11.01/22.71% of the full-aperture baselines.

When extraction results exhibit large inconsistencies, it is often informative to analyze the raw experimental S-parameters. Table 4-1 displays the measured S-parameter ranges from all three ERAM test samples. Note that due to the large loss tangent of the ERAM material, the transmission is quite low, especially for the 1.34-inch

test sample. With only 4.6% of the power transmitted through the test sample, the noise

floor of the network analyzer becomes a concern. An extraction based on only the

reflection coefficients ($S_{11}^{exp}, S_{22}^{exp}$) was attempted, but the results were not improved.

In summary, the inconsistencies in the ERAM extraction results are attributed to

three main error sources. First, the inconsistencies highlight the need for very high

quality waveguide test samples that fit into the sample holders without air gaps or

compression. Second, the ERAM foam is even more susceptible than the MRAM to

material fluctuations (i.e., inhomogeneities) across the sheet, and better results would

most likely be achieved by cutting the 2.34 and 1.34-inch test samples from the full-

aperture piece as described in the previous section. And third, the highly loaded radar

absorbing material causes a low transmitted signal-to-noise ratio, especially in the tightly

choked 1.34-inch sample holder.

Table 4-1. Experimental S-parameter ranges for ERAM (in linear power format).

2.84-inch Sample Holder	2.34-inch Sample Holder	1.34-inch Sample Holder
$0.3222 < \left\|S_{11}^{exp}\right\|^2 < 0.4708$	$0.3658 < \left\|S_{11}^{exp}\right\|^2 < 0.5133$	$0.4243 < \left\|S_{11}^{exp}\right\|^2 < 0.6873$
$0.3426 < \left\|S_{22}^{exp}\right\|^2 < 0.4773$	$0.3682 < \left\|S_{22}^{exp}\right\|^2 < 0.5060$	$0.3713 < \left\|S_{22}^{exp}\right\|^2 < 0.6345$
$0.1034 < \left\|S_{21}^{exp}\right\|^2 < 0.1657$	$0.0816 < \left\|S_{21}^{exp}\right\|^2 < 0.1333$	$0.0462 < \left\|S_{21}^{exp}\right\|^2 < 0.1175$
$0.1030 < \left\|S_{12}^{exp}\right\|^2 < 0.1652$	$0.0812 < \left\|S_{12}^{exp}\right\|^2 < 0.1328$	$0.0460 < \left\|S_{12}^{exp}\right\|^2 < 0.1170$

Figure 4-9. Permittivity of ERAM test sample mounted flush toward port two in the 2.34-inch sample holder. Maximum difference of real/imaginary permittivity is 6.55/14.02% relative to their full-aperture baselines, without considering thickness and placement uncertainties. (Permittivity only extraction using all four S-parameters.)
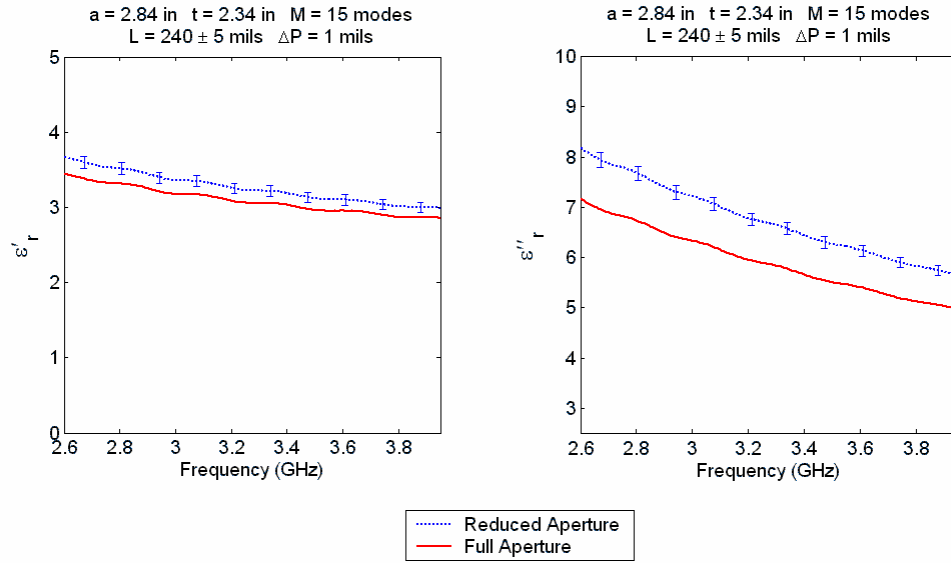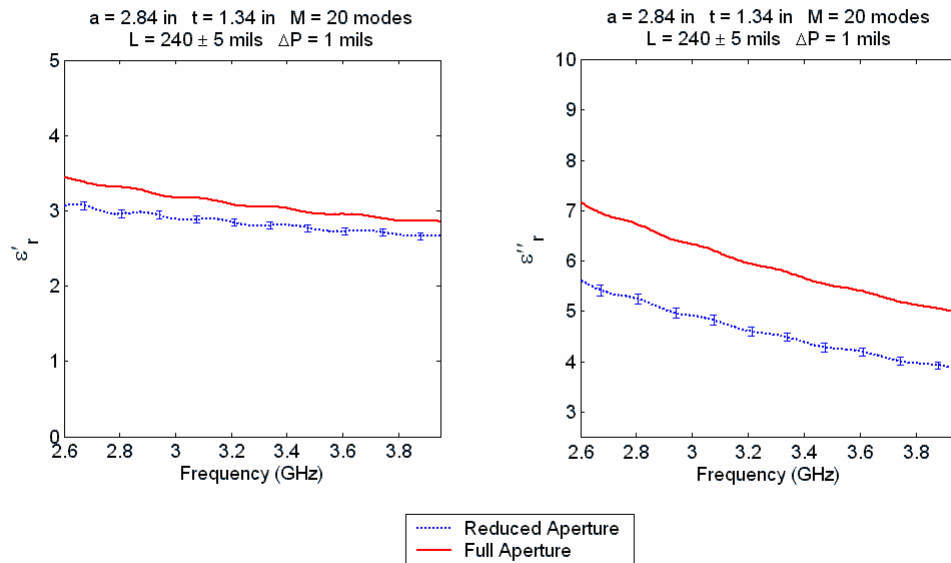

Figure 4-10. Permittivity of ERAM test sample mounted flush toward port two in the 1.34-inch sample holder. Maximum difference of real/imaginary permittivity is 11.01/22.71% relative to their full-aperture baselines, without considering thickness and placement uncertainties. (Permittivity only extraction using all four S-parameters.)

4.6 Summary

Acrylic, MRAM, and ERAM test samples mounted in reduced-width S-band sample holders were used to verify the modal analysis technique. The acrylic and MRAM results were excellent, and the ERAM results were reasonable considering the difficulties in working with the high-loss carbon-based foam. It was shown that the number of higher-order modes required for convergence is directly related to the degree of width reduction to the sample holder. Finally, a differential error analysis was presented to form error bounds related to human errors in measurement of test sample thickness and placement.

5. Conclusion and Recommendations

A stepped-waveguide technique was developed to facilitate permittivity and permeability measurement of smaller test samples in larger rectangular waveguide measurement systems. Specifically, a mode-matching technique was implemented to accommodate higher-order modes excited by the stepped junction between the waveguide feeds of the measurement system and the reduced-width sample holder. The sample permittivity and permeability were estimated by using a nonlinear least-squares algorithm to compare the theoretical S-parameters obtained from the modal analysis and the experimentally-measured S-parameters obtained from the network analyzer.

The reduced-aperture material characterization technique was experimentally verified through comparisons of stepped-waveguide measurements of acrylic, MRAM, and ERAM with traditional full-aperture, single-mode measurements. The comparisons demonstrated the validity and accuracy of the technique and also revealed that smaller apertures require a greater number of modes to achieve convergence, as anticipated. A differential error analysis conducted on test sample thickness and placement uncertainties explained most of the discrepancies from the full-aperture baselines. Finally, the high-loss ERAM demonstrated the limitations of the technique when there is poor transmission coupling combined with loose-fitting or compressed test samples.

5.1 Future Research

While experimental data from low-frequency waveguide measurements would perhaps offer insight into the best direction for future investigation, there are a few general improvements that could be made to the current reduced-width modal-analysis technique. In addition, several new modal-analysis techniques warrant investigation.

5.1.1 Possible Improvements to Current Technique.

First, the differential error analysis could be expanded to include the effects of uncertainties in more variables, such as the experimental S-parameters and sample holder dimensions. However, each additional variable uncertainty requires a separate material extraction to obtain its related error bounds, which are then added to the effects of the other variables using the triangle inequality.

Next, from a numerical standpoint, the most time-consuming part of implementing the technique is solving matrix (3.38) for the theoretical S-parameters (3.40). Investigation of a more efficient algorithm than the simple Gaussian elimination method used for this thesis would expedite the extraction process. As a reference, using a 2-GHz computer processor, a typical 20-mode least-squares extraction (involving all four S-parameters) of 201 frequency points for a 1.34-inch wide test sample takes about 2-3 minutes. Then, each variable uncertainty requires about the same extraction duration. Thus, while each extraction is by no means an all day process, analyzing several measurements can develop into a tedious endeavor.

Finally, an attenuation correction factor for the imperfectly conducting sample holder walls could be explored using a perturbation approach. Another correction factor

might also be found for air gaps between the test sample and the sample holder walls by a similar method.

5.1.2 Possible New Modal-Analysis Techniques.

A dual aperture reduction (in width and height) would allow for an additional degree-of-freedom in the machining of test samples. The accounting process for the possible excited mode shapes across the new junction geometry would have to be reinvestigated.

Also, a modal-analysis might be implemented for thin resistive sheets (R-cards) clamped directly between waveguide-feed flanges without the use of a sample holder. Copper tape could be applied around the flanges to prevent energy from escaping from the R-card to air interfaces.

Due to its higher resolution, a reduced-aperture probe might aid in detecting sub-surface defects in low-observable (LO) coatings for low-frequency radar threats. Instead of determining the material parameters, the probe would scan the surface while a real-time oscilloscope trace was monitored for sharp spikes.

On the other end of the spectrum, waveguide test sample sizes become exceedingly small for high-frequency applications. When dealing with such small test samples, machining inaccuracies and sample uniformity are important concerns. A modal-analysis technique developed for a dual aperture expansion would help alleviate these concerns by allowing a more substantial test sample to be measured and still extract the material parameters at the high frequencies of interest.

Appendix A. Proof of Matrix Relations

This appendix contains the proofs to the integral solutions given in (3.27)-(3.31).

The following trigonometric identities are used:

$$2\cos x\cos y = \cos(x+y) + \cos(x-y) \tag{A.1}$$

$$\sin(x\pm y) = \sin x\cos y \pm \cos x\sin y \tag{A.2}$$

Also, as a reminder, in the waveguide regions,

$$\vec{e}_m = \hat{y}\cos k_{xm}x \quad , \quad \vec{h}_m = \frac{\hat{z}\times\vec{e}_m}{Z_m} \quad , \quad k_{xm} = (2m-1)\pi\big/a \tag{A.3}$$

and for the ith layer in the sample holder region,

$$\vec{e}_m^{\,s} = \hat{y}\cos k_{xm}^{s}x \quad , \quad \vec{h}_m^{\,s,i} = \frac{\hat{z}\times\vec{e}_m^{\,s}}{Z_m^{s,i}} \quad , \quad k_{xm}^{s} = (2m-1)\pi\big/t \tag{A.4}$$

A.1 Integral Proofs

$$
\begin{aligned}
C_{nm} &= \int_0^{a/2} \vec{e}_n\cdot\vec{e}_m\,dx = \int_0^{a/2} \cos k_{xn}x\cos k_{xm}x\,dx \\[2mm]
&= \begin{cases} \displaystyle\int_0^{a/2}\left[\dfrac{\cos(k_{xn}+k_{xm})x}{2} + \dfrac{\cos(k_{xn}-k_{xm})x}{2}\right]dx & \dots \ m\neq n \\[4mm] \displaystyle\int_0^{a/2}\left[\dfrac{1}{2} + \dfrac{\cos 2k_{xm}x}{2}\right]dx & \dots \ m=n \end{cases} \\[4mm]
&= \begin{cases} \left[\dfrac{\sin(k_{xn}+k_{xm})x}{2(k_{xn}+k_{xm})} + \dfrac{\sin(k_{xn}-k_{xm})x}{2(k_{xn}-k_{xm})}\right]_0^{a/2} = 0 & \dots \ m\neq n \\[4mm] \left[\dfrac{x}{2} + \dfrac{\sin 2k_{xm}x}{4k_{xm}}\right]_0^{a/2} = \dfrac{a}{4} & \dots \ m=n \end{cases}
\end{aligned}
\tag{A.5}
$$

$$D_{nm} = \int_{0}^{t/2} \vec{e}_n \cdot \vec{e}_m^s \, dx = \int_{0}^{t/2} \cos k_{xn} x \cos k_{xm}^s x \, dx = \frac{\sin\left(k_{xn} + k_{xm}^s\right){}^{t}\!/_{2}}{2\left(k_{xn} + k_{xm}^s\right)} + \frac{\sin\left(k_{xn} - k_{xm}^s\right){}^{t}\!/_{2}}{2\left(k_{xn} - k_{xm}^s\right)}$$

$$= \frac{\sin{}^{k_{xn}t}\!/_{2}\cos{}^{k_{xm}^s t}\!/_{2} + \cos{}^{k_{xn}t}\!/_{2}\sin{}^{k_{xm}^s t}\!/_{2}}{2\left(k_{xn} + k_{xm}^s\right)} + \frac{\sin{}^{k_{xn}t}\!/_{2}\cos{}^{k_{xm}^s t}\!/_{2} - \cos{}^{k_{xn}t}\!/_{2}\sin{}^{k_{xm}^s t}\!/_{2}}{2\left(k_{xn} - k_{xm}^s\right)}$$

$$= \frac{k_{xn}\sin{}^{k_{xn}t}\!/_{2}\overbrace{\cos{}^{k_{xm}^s t}\!/_{2}}^{0} - k_{xm}^s\cos{}^{k_{xn}t}\!/_{2}\overbrace{\sin{}^{k_{xm}^s t}\!/_{2}}^{(-1)^{m-1}}}{k_{xn}^2 - k_{xm}^{s2}} \tag{A.6}$$

$$= \begin{cases} (-1)^m \dfrac{k_{xm}^s \cos{}^{k_{xn}t}\!/_{2}}{k_{xn}^2 - k_{xm}^{s2}} & \ldots \ k_{xm}^s \neq k_{xn} \\[2em] \dfrac{t}{4} & \ldots \ k_{xm}^s = k_{xn} \end{cases}$$

$$F_{nm} = Z_n^s \int_{0}^{t/2} \vec{h}_n^s \cdot \vec{h}_m \, dx = \frac{1}{Z_m} \int_{0}^{t/2} \hat{z} \times \vec{e}_n^s \cdot \hat{z} \times \vec{e}_m \, dx = \frac{1}{Z_m} \int_{0}^{t/2} \vec{e}_n^s \cdot \vec{e}_m \, dx$$

$$= \begin{cases} (-1)^n \dfrac{k_{xn}^s}{Z_m} \dfrac{\cos{}^{k_{xm}t}\!/_{2}}{k_{xm}^2 - k_{xn}^{s2}} & \ldots \ k_{xm} \neq k_{xn}^s \\[2em] \dfrac{t}{4Z_m} & \ldots \ k_{xm} = k_{xn}^s \end{cases} \tag{A.7}$$

$$P_{nm} = Z_n^s \int_{0}^{t/2} \vec{h}_n^s \cdot \vec{h}_m^{s,1} \, dx = \frac{1}{Z_m^{s,1}} \int_{0}^{t/2} \vec{e}_n^s \cdot \vec{e}_m^s \, dx$$

$$= \begin{cases} 0 & \ldots \ m \neq n \\[1.5em] \dfrac{t}{4Z_m^{s,1}} & \ldots \ m = n \end{cases} \tag{A.8}$$

$$Q_{nm} = Z_n^s \int_{0}^{t/2} \vec{h}_n^s \cdot \vec{h}_m^{s,N} \, dx = \frac{1}{Z_m^{s,N}} \int_{0}^{t/2} \vec{e}_n^s \cdot \vec{e}_m^s \, dx$$

$$= \begin{cases} 0 & \ldots \ m \neq n \\[1.5em] \dfrac{t}{4Z_m^{s,N}} & \ldots \ m = n \end{cases} \tag{A.9}$$

References

[1]   A. M. Nicolson and G. F. Ross, "Measurement of the intrinsic properties of materials by time-domain techniques," *IEEE Trans. Instrum. Meas.*, vol. IM-19, pp. 377-382, Nov. 1970.

[2]   W. B. Wier, "Automatic measurement of complex dielectric constant and permeability at microwave frequencies," *Proc. IEEE*, vol. 62, pp. 33-36, Jan. 1974.

[3]   W. Barry, "A broad-band, automated, stripline technique for the simultaneous measurement of complex permittivity and permeability," *IEEE Trans. Microwave Theory Tech.*, vol. 34, pp. 80-84, Jan. 1986.

[4]   J. Baker-Jarvis, E. J. Vanzura, and W. A. Kissick, "Improved technique for determining complex permittivity with the transmission/reflection method," *IEEE Trans. Microwave Theory Tech.*, vol. 38, pp. 1096-1103, Aug. 1990.

[5]   M. J. Havrilla, "Analytical and experimental techniques for the electromagnetic characterization of materials," Ph.D. dissertation, Michigan State University, 2001.

[6]   R. E. Collin, *Field Theory of Guided Waves*, 2nd ed. New York: IEEE Press, 1991.

[7]   C. A. Balanis, *Advanced Engineering Electromagnetics*. New York: John Wiley & Sons, 1989.

[8]   R. E. Collin, *Foundations for Microwave Engineering*, 2nd ed. New York: IEEE Press, 2001.

[9]   D. M. Pozar, *Microwave Engineering*, 2nd ed. New York: John Wiley & Sons, 1998.

[10]   R. F. Harrington, *Field Computation by Moment Methods*. New York: Macmillan, 1968.

REPORT DOCUMENTATION PAGE

The public reporting burden for this collection of information is estimated to average 1 hour per response, including the time for reviewing instructions, searching existing data sources, gathering and maintaining the data needed, and completing and reviewing the collection of information. Send comments regarding this burden estimate or any other aspect of the collection of information, including suggestions for reducing this burden to Department of Defense, Washington Headquarters Services, Directorate for Information Operations and Reports (0704-0188), 1215 Jefferson Davis Highway, Suite 1204, Arlington, VA 22202-4302. Respondents should be aware that notwithstanding any other provision of law, no person shall be subject to an penalty for failing to comply with a collection of information if it does not display a currently valid OMB control number.
LEASE DO NOT RETURN YOUR FORM TO THE ABOVE ADDRESS.

1. REPORT DATE *(DD-MM-YYYY)* 23-03-2004	2. REPORT TYPE Master's Thesis	3. DATES COVERED *(From - To)* January 2003 – March 2004

4. TITLE AND SUBTITLE
STEPPED WAVEGUIDE ELECTROMAGNETIC MATERIAL CHARACTERIZATION TECHNIQUE

5a. CONTRACT NUMBER

5b. GRANT NUMBER

5c. PROGRAM ELEMENT NUMBER

6. AUTHOR(S)
Dorey, Sean P., Captain, USAF

5d. PROJECT NUMBER

5e. TASK NUMBER

5f. WORK UNIT NUMBER

7. PERFORMING ORGANIZATION NAME(S) AND ADDRESS(ES)
Air Force Institute of Technology
Graduate School of Engineering and Management (AFIT/EN)
2950 Hobson Way; Bldg. 640
WPAFB OH 45433-7765

8. PERFORMING ORGANIZATION REPORT NUMBER

AFIT/GEO/ENG/04-01

9. SPONSORING/MONITORING AGENCY NAME(S) AND ADDRESS(ES)
AFRL/SNS (AFMC)
Attn: George R. (Bob) Simpson, Ph.D.
2591 K Street; Bldg. 254
WPAFB, OH 45433-7602
(937) 255-9288   george.simpson@wpafb.af.mil

10. SPONSOR/MONITOR'S ACRONYM(S)

11. SPONSOR/MONITOR'S REPORT NUMBER(S)

12. DISTRIBUTION AVAILABILITY STATEMENT
APPROVED FOR PUBLIC RELEASE; DISTRIBUTION UNLIMITED

13. SUPPLEMENTARY NOTES

14. ABSTRACT
  Electromagnetic material characterization is the process of determining the complex permittivity and permeability of a material. A new waveguide material measurement technique is developed to reduce test sample size requirements for low-frequency applications. Specifically, a waveguide sample holder having a reduced aperture is utilized to decrease the time and cost spent producing large precision test samples. This type of sample holder causes a disruption in the waveguide-wall surface currents that results in the excitation of higher-order modes. This thesis will demonstrate how these higher-order modes can be accommodated using a modal-analysis technique, thus resulting in the ability to measure smaller samples mounted in large waveguides and still determine the constitutive parameters of the materials at the desired frequencies.
  Experimental results for acrylic and magnetic and electric radar absorbing materials are compared to ideal full-aperture measurements at S-band (2.6 -3.95 GHz) to verify the modal-analysis technique. In addition, since uncertainties in test sample thickness and placement are predominantly encountered in material characterization measurements, a differential error analysis is performed to determine associated error bounds.

15. SUBJECT TERMS
Stepped Waveguide, Waveguide Discontinuities, Electromagnetic Material Characterization, Modal Analysis

16. SECURITY CLASSIFICATION OF:			17. LIMITATION OF ABSTRACT	18. NUMBER OF PAGES	19a. NAME OF RESPONSIBLE PERSON Dr. Michael J. Havrilla
a. REPORT U	**b. ABSTRACT** U	**c. THIS PAGE** U	UU	63	**19b. TELEPONE NUMBER** *(Include area code)* (937) 255-3636 x4582 (michael.havrilla@afit.edu)

Standard Form 298 (Rev. 8-98)
Prescribed by ANSI-Std Z39.18